

Detecting active latitudes of Sun-like stars using asteroseismic a-coefficients

Othman Benomar¹²³, Masao Takata⁴, Michael Bazot⁵, Takashi Sekii¹², Laurent Gizon³⁶⁷, and Yuting Lu⁸

¹ Department of Astronomical Science, School of Physical Sciences, SOKENDAI, 2-21-1 Osawa, Mitaka, Tokyo 181-8588 e-mail: othman.benomar@nao.ac.jp, ob19@nyu.edu

² Solar Science Observatory, National Astronomical Observatory of Japan, 2-21-1 Osawa, Mitaka, Tokyo 181-8588, Japan

³ New York University Abu Dhabi, Center for Space Science, PO Box 129188, UAE

⁴ Department of Astronomy, School of Science, The University of Tokyo, 7-3-1 Hongo, Bunkyo-ku, Tokyo, 113-0033, Japan

⁵ Heidelberg Institut für Theoretische Studien, Schloss-Wolfsbrunnenweg 35, 69118 Heidelberg, Germany

⁶ Max-Planck-Institut für Sonnensystemforschung, 37077, Göttingen, Germany

⁷ Institut für Astrophysik, Georg-August-Universität Göttingen, 37077, Göttingen, Germany

⁸ Department of Physics, The University of Tokyo, Tokyo 113-0033, Japan

Received 30 May 2023 Accepted July 19, 2023

ABSTRACT

Aims. We introduce a framework to measure the asphericity of Sun-like stars using a_1 , a_2 and a_4 coefficients, **and constrain their latitudes of magnetic activity**.

Methods. Systematic errors on the **inferred** coefficients are evaluated in function of key **physical and seismic parameters** (inclination **of rotation axis**, average rotation, height-to-noise ratio **of peaks in power spectrum**). **The measured a-coefficients account for rotational oblateness and the effect of surface magnetic activity. We use a simple model that assumes a single latitudinal band of activity.**

Results. Using solar SOHO/VIRGO/SPM data, we demonstrate the capability of the method to detect the mean active latitude and its intensity changes between 1999-2002 (maximum of activity) and 2006-2009 (minimum of activity). We further apply the method to study the solar-analog stars 16 Cyg A and B using Kepler observations. An equatorial band of activity, exhibiting intensity that could be comparable to that of the Sun, is detected in 16 Cyg A. However, 16 Cyg B exhibits a bi-modality in a_4 that is challenging to explain. We suggest that this could be a

manifestation of the transition between a quiet and an active phase of activity. Validating or invalidating this hypothesis may require new observations.

Key words. stars:activity, stars:rotation, stars:solar-type, asteroseismology

1. Introduction

The observations from the space-borne instruments MOST (Walker et al. 2003), CoRoT (Baglin et al. 2006), *Kepler* (Borucki et al. 2010) and TESS (Ricker et al. 2014) have been important in advancing our knowledge of stellar interiors. This is particularly true for *Kepler*, which could observe continuously tens of thousand of stars for nearly four continuous years, enabling asteroseismic measurements that almost rival disk-integrated helioseismic measurements from a decade ago. Those precise measurements have for example enabled us to better understand stellar rotation and its impact on stellar evolution. The asteroseismology of Sun-like stars is based on the study of the pressure modes that are excited by turbulent convection in the outer layers of these stars. The acoustic modes may reach deep into the core or may be localised close to the stellar surface, giving access to the internal structure and dynamics of the stars. Rotation has a critical impact on the stellar structure and evolution as it induces a material mixing process (Maeder & Meynet 2008). Rotation is also an essential ingredient of the dynamo-effect (Thompson et al. 2003) and can lead to a distortion of the star's shape due to the centrifugal force (Chandrasekhar 1969). For fast rotators, the rotational flattening must be taken into account. These stars show a variety of pulsation modes that are not present in slower rotators (e.g. Lignières et al. 2006).

Despite its slow rotation rate, the solar asphericity can be measured by helioseismology. While the Sun is seen as oblate by acoustic modes during the quiet phases of its activity cycle, the modes feel a more complicated shape during activity maxima. During solar maxima, the frequencies of acoustic modes increase slightly due to the presence of active regions. The perturbation occurs near the surface and is stronger for modes that sense the active latitudes (below $\approx 30^\circ$ for the Sun). Physically the magnetic perturbations consist of several components that are not easy to disentangle (incl. stratification and wave speed perturbations (Libbrecht & Woodard 1990; Antia et al. 2000; Dziembowski et al. 2000). The magnetic perturbations affect the acoustic modes near the surface over only a few hundred kilometers, that is of order $10^{-5} R_\odot$, but is significant enough to be measured.

The origin of stellar activity is not well understood as it depends on the complex interplay between rotation, convection and the magnetic field (Brun & Browning 2017). Stellar magnetic cycles are observed in most cool stars (Simon et al. 2002) over a large range of the electromagnetic spectrum and evidence of activity cycles is observed in X-ray (eg. Catura et al. 1975), radio waves (White 1999; White et al. 2017), chromospheric emission lines (Vaughan 1983; Oláh et al. 2009, 2016), and also through luminosity variation due to surface magnetic activity in the visible (Hartmann & Rosner 1979; Silva-Valio et al. 2010; Ceillier et al. 2017). On Sun-like stars, the

level of activity is often observed to be cyclic, with activity periods ranging from a few years to decades. Although there are relationships between the stellar age, the rotation period, and the level of activity (van Saders et al. 2016), the underlying mechanisms at play are not understood.

Since the advent of space-borne photometry and the observation of Sun-like pulsators by CoRoT, it became evident that helioseismic methods used for the Sun may be applied to asteroseismic observations. This has resulted in robust estimates of the average rotational splittings, which, in combination with the surface rotation rates inferred from photometric variability, indicate that main sequence stars have nearly-uniform internal rotation rates, (Gizon et al. 2013; Benomar et al. 2015; Nielsen et al. 2017). **All of the recent seismic studies of radial differential rotation agree that angular momentum transport in the radiative zone is much more efficient than considered in theory, even in the case of stars more massive than Sun-like stars, such as γ -Doradus stars (eg. Mosser et al. 2012; Gehan et al. 2018; Ouazzani et al. 2019).** For the best Kepler observations, asteroseismology showed evidence of latitudinal differential rotation for main sequence stars (Benomar et al. 2018a) and of the radial differential rotation in RGB (e.g. Deheuvels et al. 2012, 2014).

This paper aims at providing a framework to study stellar activity and its latitude by analysing its effect on pulsation frequencies. The proposed method involves the use of the *a*-coefficient decomposition (Schou et al. 1994; Pijpers 1997, 1998) on the stellar power spectrum, conveniently separating the perturbations caused by rotation and asphericity. The method is tested on Sun-as-a-star data and on the solar-analogs 16 Cyg A and B, which are the two brightest stars in the initial Kepler observation field.

Only few successful measurements of the asphericity of other stars than the Sun have been made so far. Using ultra-precise measurements of the frequency splittings of time-harmonic (i.e. non-stochastic) low-degree p-modes, Gizon et al. (2016) inferred the oblateness of the γ Doradus– δ Scuti star KIC 11145123 to be $\Delta R = (1.8 \pm 0.6) \times 10^{-6} R \simeq 3 \pm 1$ km, i.e. smaller than expected from rotational oblateness alone, suggesting the presence of magnetic activity at low latitudes. Bazot et al. (2019) measured the asphericity of the solar-like pulsators 16 Cyg A and B and found that 16 Cyg A is likely prolate, implying that this star may have low-latitude magnetic activity on its surface.

In the spirit of the study by Gizon (2002), we will perform monte-carlo simulations to demonstrate the possibility of inferring the even-*a* coefficients from simulated oscillation power spectra to constrain the latitude of activity. Unlike Gizon (2002) who included only the a_2 coefficient in the parametric model, we will infer both the a_2 and a_4 coefficients. We start in Section 2 by introducing the effects of rotation on pulsation frequencies and discuss the effect of the centrifugal force and of the activity on the mode cavities. Section 3 presents the assumptions required for the asteroseismic measurement of stellar activity. Section 4 discusses the achievable accuracy of the seismic observables, while sections 5 and 6 present the results on solar data and for 16 CygA and B. This is followed by a discussion and conclusion in section 7.

72 2. The effect of rotation and of magnetic activity

73 This section presents the effect of rotation and of magnetic activity on pulsation modes, and intro-
 74 duces the frequency model used for asteroseismic data analysis.

75 2.1. Frequency splittings

76 Slowly rotating stars without significant magnetic activity are approximately spherical and it is
 77 common to describe the family of modes traveling inside it using spherical harmonics (see e.g.
 78 Unno et al. 1989). If the departure from sphericity remains small enough, it is convenient to keep
 79 the spherical representation for the equilibrium model and account for distortions through a per-
 80 turbation analysis. All pulsations can then be described using a set of integers (n,l,m) , namely
 81 the radial order, the mode degree and the azimuthal order, respectively. Acoustic pressure modes
 82 observed in Sun-like stars can be identified using their frequencies ν_{nlm} .

83 In a non-rotating, non-active star, m-components are degenerate and cannot be resolved. When
 84 rotation or magnetic activity sets in, this degeneracy is lifted. The resulting frequency is treated as
 85 a perturbation to the degenerate frequency without rotation and activity,

$$\nu_{nlm} = \nu_{nl} + \delta\nu_{nlm}, \quad (1)$$

86 with ν_{nl} , the equilibrium eigenfrequency without rotation and activity and $\delta\nu_{nlm}$ the frequency split-
 87 ting. These splitting may depend on multiple physical effects perceived by the modes (Libbrecht
 88 & Woodard 1990) within their cavity of propagation. These can be terms of order $O(\Omega)$, with Ω
 89 the rotation rate estimated at the equator, $\Omega = \Omega(r, \theta = \pi/2)$. These depend directly on the stellar
 90 rotation profile $\Omega(r, \theta)$. Higher-order perturbations pertaining to the shape of the mode cavity can
 91 also exist. Note that ν_{nl} differs from $\nu_{nl, m=0}$ as the $m = 0$ components may have their frequency
 92 shifted by perturbations such as the magnetic activity (see e.g. Figure 1).

93 Splitting can be described using the Clebsch-Gordan a-coefficient decomposition (Ritzwoller
 94 & Lavelle 1991), that corresponds to a representation of the splittings on a basis of polynomials
 95 $\mathcal{P}_j^{(l)}(m)$ of degree j in m ,

$$\delta\nu_{nlm} = \sum_{j=1}^{j_{max}} a_j(n, l) \mathcal{P}_j^{(l)}(m), \quad (2)$$

96 with the polynomials such that

$$\sum_{m=-l}^l \mathcal{P}_i^{(l)}(m) \mathcal{P}_j^{(l)}(m) = 0 \text{ when } i \neq j. \quad (3)$$

97 Here, $a_j(n, l)$ is the a-coefficient of order j and $j_{max} = 2l$ is the maximum order to which the
 98 decomposition must be carried for a given degree. The standard set of polynomials used in this
 99 expansion are those normalized as per described by Schou et al. (1994).

This decomposition is extensively used in helioseismology and was used on Sun-like stars by Benomar et al. (2018a). Asteroseismology has been so far unable to observe modes of degree higher than $l = 3$ so that in the following the discussion is restricted to $l \leq 3$ and $j_{max} = 2l = 6$, due to the selection rule of the $\mathcal{P}_j^{(l)}(m)$. This limitation is the consequence of full-disk integrated photometric observations. An example of splitting including odd and even a_j coefficients is given in Figure 1 for $l = 1, 2$.

This theoretical model leads to a natural interpretation of the observed splittings. One may decomposes these latter into their symmetrical, S_{nlm} , and anti-symmetrical, T_{nlm} , parts. These components can then be described as sums over, respectively, the odd and even a-coefficients,

$$S_{nlm} = \frac{\nu_{n,l,m} - \nu_{n,l,-m}}{2m} = \frac{1}{m} \sum_{j=1}^{j_{max}/2} a_{2j-1}(n, l) \mathcal{P}_{2j-1}^{(l)}(m), \quad (4)$$

$$T_{nlm} = \frac{\nu_{n,l,m} + \nu_{n,l,-m}}{2} - \nu_{n,l,0} = \sum_{j=1}^{j_{max}/2} a_{2j}(n, l) (\mathcal{P}_{2j}^{(l)}(m) - \mathcal{P}_{2j}^{(l)}(0)). \quad (5)$$

This arises from the parity relation $\mathcal{P}_j^{(l)}(-m) = (-1)^j \mathcal{P}_j^{(l)}(m)$. These equations can be used to express the a-coefficients with S_{nlm} and T_{nlm} . They also provide relations between the ν_{nlm} with the $a_j(n, l)$ (Appendix A.2).

It can be seen from Appendix A.1 that the sums in Eqs. (4) and (5) involve, respectively, odd and even functions of m . Physically, this means that the symmetrical components of the splittings (Gough & Thompson 1990) result from large-scale perturbations sensitive to the prograde or retrograde nature of the waves, such as advection or the Coriolis force. On the other hand, the anti-symmetric splittings are caused by processes that are not affected by the propagation direction of waves. This may include the centrifugal force, that scales as $O(\Omega^2)$, and whose effect on the oscillation frequencies varies as m^2 . Magnetic fields or non-spherical deformations of the equilibrium structure will also contribute to the anti-symmetric splittings.

We further decompose the anti-symmetric splittings into a term depending on centrifugal-force-induced distortions and another one accounting for activity-related distortions,

$$T_{nlm} = \delta\nu_{nlm}^{(CF)} + \delta\nu_{nlm}^{(AR)}. \quad (6)$$

The symmetric part of the splitting corresponds to a term $\delta\nu_{nlm}^{(rot)}$ that stems from perturbations of order $O(\Omega)$ and the total observed splitting is,

$$\delta\nu_{nlm} = \delta\nu_{nlm}^{(rot)} + \delta\nu_{nlm}^{(CF)} + \delta\nu_{nlm}^{(AR)}. \quad (7)$$

Using the Sun as an archetype of Sun-like star, it is possible to measure these contributions to $\delta\nu_{nlm}$ as shown in Sections 2.2 and 2.3.

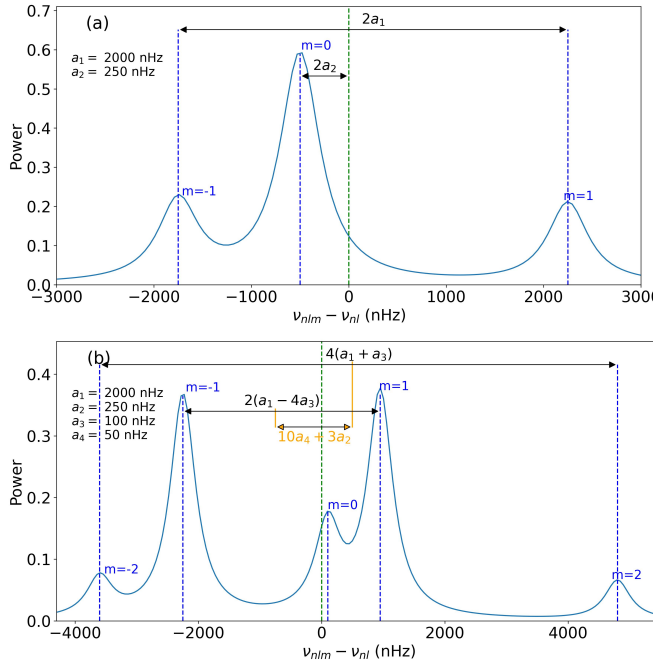


Fig. 1. Example of Lorentzian mode profiles showing the a-coefficients and their relationship with frequencies spacings for $l = 1$ (a) and $l = 2$ modes (b). The orange spacing is $T_{n22} - T_{n21}$. v_{nl} is the m-averaged frequency of each multiplet. The stellar inclination is 40° .

126 2.2. Expressions for $\delta\nu_{nlm}^{(rot)}$, $\delta\nu_{nlm}^{(CF)}$ and $\delta\nu_{nlm}^{(AR)}$

127 To the first order, the perturbation on the frequency due to rotation is,

$$\delta\nu_{nlm}^{(rot)} = \frac{m}{2\pi} \int_0^R \int_0^\pi K_{nlm}(r, \theta) \Omega(r, \theta) r dr d\theta, \quad (8)$$

128 where R is the radius of the star and the kernel $K_{nlm}(r, \theta)$ (Hansen et al. 1977) expresses the sensitivity of a mode to the rotation at the radial point r and co-latitude θ . $\Omega(r, \theta)$ is the rotation profile of the star. It can be shown that $\delta\nu_{nlm}^{(rot)}$ actually only depends on symmetrical splittings (Ritzwoller & Lavey 1991) which in turns depend only on odd coefficients. For example and for $l = 3$, it is expressed as,

$$\delta\nu_{nlm}^{(rot)} \simeq \mathcal{P}_1^{(l)}(m) a_1 + \mathcal{P}_3^{(l)}(m) a_3 + \mathcal{P}_5^{(l)}(m) a_5. \quad (9)$$

133 Centrifugal forces typically distort a spherical rotating sphere of gas into an oblate ellipsoid, elongated at the equator. Functional analysis shows that the contribution of centrifugal forces to 134 the mode splitting scales with $\Omega^2 R^3 / GM$. Properly integrating higher-order terms of the perturbation expansion over the aspherical volume of the star and using asymptotic expressions for the 135 equilibrium mode eigenfunctions (assuming n is large enough), leads to the following expression 136 for the centrifugal-force component of the frequency splitting (Gough & Taylor 1984; Gough & 137 Thompson 1990),

$$\delta\nu_{nlm}^{(CF)} = \frac{\Omega^2 R^3}{GM} v_{nl} Q_{lm}, \quad (10)$$

with $Q_{lm} \approx \frac{2}{3} \frac{l(l+1)-3m^2}{(2l-1)(2l+3)}$ factor depending on the density. Equation (10) means that 140

$$\delta\nu_{nlm}^{(CF)} = \mathcal{P}_2^{(l)}(m) a_2^{(CF)}(n, l) \quad (11)$$

with 141

$$a_2^{(CF)}(n, l) = -\frac{1}{2l+3} \frac{\Omega^2 R^3}{GM} \nu_{nl} \quad (12)$$

since $-(2l+3)Q_{lm} = \mathcal{P}_2^{(l)}(m)$. It should be noted that the contribution of the centrifugal-force-induced deformation to the frequency splittings can be described by a linear combination of the \mathcal{P}_{2j} polynomials (Gough & Taylor 1984; Gough & Thompson 1990). Since the stars are assumed to be slowly rotating, one may only retain terms of order $O(\Omega^2)$, which correspond to the contribution of the a_2 coefficient alone. 142
143
144
145
146

One can further approximate equation (12) in order to express $\delta\nu_{nlm}^{(CF)}$ as a function of quantities that can be obtained directly from the modeling of the acoustic power spectra of Sun-like stars (Benomar et al. 2018a). First, the **stellar mean density** of a Sun-like star scales to a good approximation with its large separation, that is the average distance in the frequency space between two modes of identical degree and consecutive orders (Ulrich 1986). In solar units, this reads $\rho = (\rho_\odot/\Delta\nu_\odot)\Delta\nu$, with the solar density $\rho_\odot = (1.4060 \pm 0.0005) \times 10^3 \text{ kg m}^{-3}$ and $\Delta\nu_\odot = 135.20 \pm 0.25 \mu\text{Hz}$ (García et al. 2011b). With an accuracy estimated to a few percents for Sun-like stars (White et al. 2011), the use of this scaling relation is thought to be a decent approximation. 147
148
149
150
151
152
153
154

The second simplification uses the fact that the Clebsch-Gordan coefficient decomposition of the frequency splitting imposes a one-to-one relationship between the a-coefficients and the coefficients of the decomposition of the velocity field into poloidal and toroidal components (Ritzwoller & Lavelle 1991). Helioseismology suggests that the Sun rotates with a near constant angular velocity down to at least $r/R_\odot = 0.2$ (e.g. Thompson et al. 2003), which is the maximum depth at which measurements from low-degree p modes are available. Furthermore, its outer-convective zone shows a differential rotation of $\simeq 30\%$ from the equator to the pole, which leads to an $a_{3,\odot}(n, l) \simeq 4 \text{ nHz}$ and to even smaller values for higher odds a-coefficients. This is significantly smaller than $a_{1,\odot}(n, l) \simeq 420 \text{ nHz}$. Therefore, the aforementioned one-to-one relation ensures that we can retain only the leading order in the expansion of the rotation rate and treat it as an average value, given in terms of seismic observables by $\Omega \simeq 2\pi a_1$. This leads to 155
156
157
158
159
160
161
162
163
164
165

$$a_2^{(CF)}(n, l) \simeq -\frac{\nu_{nl}}{2l+3} \frac{3\pi}{G\rho_\odot} \frac{\Delta\nu_\odot^2}{\Delta\nu^2} a_1^2. \quad (13)$$

166

Regarding $\delta\nu_{nlm}^{(AR)}$, there is no unambiguous theory to describe the effect of the near-surface magnetic activity on the shape of the cavity. Due to this and following Gizon (2002), a geometrical description is preferred to a physical model. This description assumes that the corresponding wave-speed perturbation separates in the latitudinal and radial coordinates. The proposed form of the 167
168
169
170

171 perturbation in frequency is,

$$\begin{aligned}\delta\nu_{nlm}^{(AR)} &= \nu_{nl}\epsilon_{nl} \int_0^{2\pi} \int_0^\pi F(\theta|\mathbf{x})|Y_l^m(\theta, \phi)|^2 \sin \theta d\theta d\phi \\ &= \nu_{nl}\epsilon_{nl}A_{lm}(\mathbf{x}) \\ &= \sum_{j=0}^{j_{\max}/2} \mathcal{P}_{2j}^{(l)}(m) a_{2j}^{(AR)}(n, l).\end{aligned}\quad (14)$$

172 The term $a_{2j}^{(AR)}(n, l)$ in equation (14) refers to the combined contribution of a magnetic field and
 173 other perturbations in the stellar **structure** (e.g. stratification, temperature). The geometrical weight
 174 function $A_{lm}(\mathbf{x})$ describes the effect of an active zone at the co-latitude θ , on a mode of degree l
 175 and azimuthal order m . $A_{lm}(\mathbf{x})$ is the product of two contributions. First, the normalized spheri-
 176 cal harmonics $Y_l^m(\theta, \phi)$ that decompose the magnetic activity effect over each modes. These are
 177 spherical-polar coordinates defined in the inertial frame with a polar axis pointing in the direction
 178 of the rotation axis. Second, the weight distribution (or the shape of the active region) is defined by
 179 $F(\theta|\mathbf{x})$. Here, \mathbf{x} refers to the parameters that are necessary to describe the function $F(\theta|\mathbf{x})$.

180 On the Sun, large active regions persist on the surface for 1-2 rotation periods and are ran-
 181 domly distributed in longitude over well defined latitudes. Here we assume that the corresponding
 182 perturbation can be approximated by a function of latitude only. The general problem of distinct
 183 active regions on the differentially rotating surface would go beyond the present study (see Papini
 184 & Gizon 2019, for the case of a single long-lived active region). In this paper, we only consider
 185 perturbations that are approximately steady in the inertial frame (i.e. latitudinal bands of activity).

186 In theory, a third integral over the radius is necessary to describe the dependence of the mag-
 187 netic activity to the stellar depth. However, p modes are weakly sensitive to the deep structure
 188 inside stars. Here, the radial integral is replaced by ϵ_{nl} , the overall activity intensity. The frequency
 189 ν_{nl} allows a dimensionless ϵ_{nl} , that can be compared between stars. Section 3.2 further develops
 190 the required assumptions in order to obtain a reliable information content on the active region in
 191 asteroseismology.

192 2.3. Modeling the frequencies

193 Combining equation (1), (7), (8), (13) and (14) leads to,

$$\begin{aligned}\nu_{nlm} &= \nu_{nl} \left(1 + \frac{3\pi}{(2l+3)\mathcal{G}\rho_\odot} \frac{\Delta\nu_\odot^2}{\Delta\nu^2} a_1^2 \right) \\ &+ \epsilon_{nl}A_{lm}(\mathbf{x}) + \frac{m}{2\pi} \int_0^R \int_0^\pi K_{nlm}(r, \theta) \Omega(r, \theta) r dr d\theta.\end{aligned}\quad (15)$$

Using equation (1) and (2), ν_{nlm} can also be expressed using the a-coefficients without loss of generality. 194
generality. 195

$$\nu_{nlm} = \nu_{nl} + \sum_{j=1}^{2l} \mathcal{P}_j^{(l)}(m) a_j(n, l). \quad (16)$$

It is possible to use equation (15) in order to measure the activity parameters \mathbf{x} , by directly fitting the power spectrum. However, there are multiple benefits to use instead a two-step approach consisting in first using equation (16) for the fitting of the power spectrum to evaluate the a-coefficients (method **detailed** in Appendix B). And then, fitting the coefficients obtained during the first step, using solely the equations (13) and (14) (**detailed** in Appendix C). Firstly and in the general case, the evaluation of $A_{lm}(\mathbf{x})$ requires the precise computation of a double integral. This is a slow process, that increases the time necessary to fit the power spectrum¹. Postponning to an ulterior step the computation of $A_{lm}(\mathbf{x})$ reduces drastically the parameter space from a few tens of parameters to only a few², effectively making faster the convergence rate of the fitting algorithm and making it easier to explore the assumptions that have to be made on equation (15) in order to have a functional approach in real cases (see the discussions in Section 3). Secondly, it allows us to decouple the observables from the physics, enabling to test various physical assumptions without having to re-perform the lengthy power spectrum analysis. Finally, it eases the evaluation of the reliability of the activity determination, by enabling us to pinpoint the cause of biases (if any) on either the observables (eg. a_2 , a_4 , see Section 4) or on the interpretation of these observables in terms of physical parameters (see Section 3.3). The disadvantage of the two-step approach is that it requires more statistical assumptions, such as negelecting correlations and assuming Gaussian parameters. Although one can argue that it is possible to perform a hierarchical Bayesian analysis (eg. Hogg et al. 2010; Campante et al. 2016) to partly alleviate this issue, such an approach is generally slow and may cancel the benefits of the two-step approach.

3. Information content in low order a-coefficients

The general theoretical formulations of Section 2, demonstrate how pulsation frequencies are expressed as function of the rotation, the centrifugal distortion and the activity of stars. However, observational limitations need to be accounted to enable a viable, robust model that extract as much possible the information content within currently existing data. This necessarily requires additional assumptions, for which the rational is **detailed** hereafter. 216
assumptions, for which the rational is **detailed** hereafter. 217
assumptions, for which the rational is **detailed** hereafter. 218
assumptions, for which the rational is **detailed** hereafter. 219
assumptions, for which the rational is **detailed** hereafter. 220
assumptions, for which the rational is **detailed** hereafter. 221

3.1. Factors contributing to the splitting accuracy and precision

As explained in Kamiaka et al. (2018), the pulsation height (H) and the noise background (N) are important factors that reduce the capabilities of asteroseismic analyses. Those are a complex 222
As explained in Kamiaka et al. (2018), the pulsation height (H) and the noise background (N) 223
are important factors that reduce the capabilities of asteroseismic analyses. Those are a complex 224

¹Using a MCMC method, from a day to a couple of weeks for a single star on a present-day CPU

²With our choice of $A_{lm}(\mathbf{x})$, three parameters are fitted. See section 3.2.

function of the global stellar characteristics (mass, radius, age), of the convective motion at the surface of Sun-like stars, and also depend on the instrumental limitations. The mode height and the noise background are in fact difficult to evaluate *a priori*. However, the Height-to-Noise (HNR), defined as the ratio H/N can be used to **assess** the quality of the spectrum of a pulsation mode. In fact, Kamiaka et al. (2018) show that the HNR at maximum of mode height \widehat{HNR} , can be used to study biases on the stellar inclination. This is because all main sequence Sun-like stars show a similar dependency of the height and of the width as a function of the frequency (see e.g. Appourchaux et al. 2014). In Section 4, we propose the same, but on a-coefficients.

The \widehat{HNR} not only defines how many modes can be observed, but also the maximum degree of the modes that is observed. Considering specifically the Kepler observations, stars exhibit a \widehat{HNR} for $l = 0$ modes of up to 30, the highest HNR being observed for 16 Cyg A and 16 Cyg B. Kamiaka et al. (2018) showed that the capability of distinguishing rotationally split components is of great importance if one wants to obtain a reliable asteroseismic inference of the rotation characteristics and of the stellar inclination. In particular, the ratio $a_1/\Gamma_{\nu_{max}}$ between the a_1 coefficient and the mode width determined at the maximum of mode amplitude $\Gamma_{\nu_{max}}$ (see Figure 6), determines the expected bias on the stellar inclination. As shown in Section 4, $a_1/\Gamma_{\nu_{max}}$ also controls the importance of the bias for the other low order a-coefficients. Finally, another important factor is the spectrum resolution. The higher the resolution, the more resolved are the modes. Thus, observations T_{obs} of several years are the most suitable in order to resolve and measure rotationally split components. Broadly speaking, observations exceeding a year and $a_1/\Gamma > 0.4$ are preferable to ensure a reliable measurement of a_1 .

All of the limitations discussed above incite us to introduce assumptions to ensure robust measurements of a-coefficients (ie, mitigate biases).

3.2. Latitudinal profile of the activity

Noting that it is challenging to measure low-degree a-coefficients for the Sun (eg. Toutain & Kosovichev 2001), we present here a minimal set of assumptions on even a-coefficients allowing us to constrain the asphericity of stellar cavities. One of the first aspects that has to be considered is the form of $F(\theta|\mathbf{x})$, the function characterising the activity latitude θ (see equation (14)).

The butterfly diagram of the Sun (Figure 2) is used as a reference for this latitudinal dependence. The data are from the Greenwich USAF/NOAA observatory (<https://solarscience.msfc.nasa.gov/greenwch.shtml>) and provide the daily area of the spots, counted manually over the period 1874-2016. The panel (a) on Figure 2 shows the butterfly diagram with colors representing the area covered by the spots in unit of percent of visible hemisphere. It focuses on the observations after 1985 and covers two full solar cycles. Vertical color bands highlight three time intervals : 1985-1989 (Purple), 1999-2002 (Blue) and 2006-2009 (Yellow). The two first are during a maximum of solar activity while the last one is for a minimum of activity. Due to the gradual migration of the spots over time, the longer observation period (1985-1989, 4 years) leads

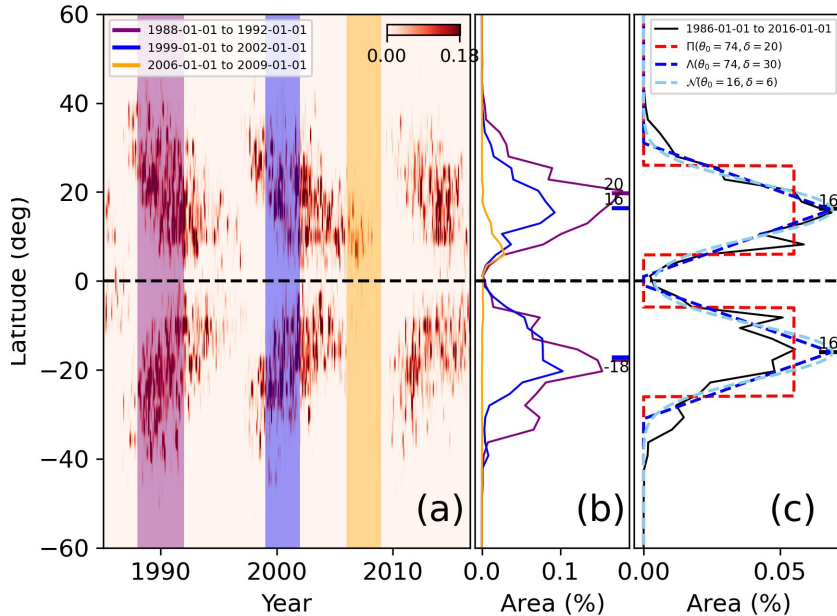


Fig. 2. (a) Butterfly diagram for the Sun. Vertical color bands highlight periods of maximum of 1988-1992, 1999-2002 and minimum of activity of 2006-2009. (b) averaged spot area for the highlighted periods. Colored ticks on (b) are the weighted mean for the activity latitude. (c) Filters $F(\theta|X)$ used for this study superimposed to solar data (1986-2016). Parameters θ_0 and δ are the latitude and the extension of the active region, respectively.

to a broader activity zone than the period 1999-2002. This indicates that the extension of the active region may not be trivial to measure in other stars because it will depend on the fraction of time the star is observed relative to the duration of its activity cycle. The activity cycles of Sun-like stars (if any) is a priori unknown, but Ca II H+K line emission and photometric studies (Oláh et al. 2009, 2016) suggest that it is of durations of roughly a few years to decades, as for the Sun. It indicates that over the course of several years, an active band as large as $\simeq 40^\circ$ may be expected.

Panel (b) of Figure 2 shows the cumulative area of spots as a function of the latitude and for the three considered periods. As noted earlier, the extension of the activity band is larger for the longest timeframe. The area of the spots during the active solar phase are symmetrical towards the equator. This suggests that when the activity is strong, $F(\theta|X)$ is almost north-south symmetric. This may be inaccurate for low activity phase, as shown for the period 2006-2009 but because $|Y_l^m(\theta, \phi)|^2$ is also symmetrical towards the equator, this has no incidence on the $a_j^{(AR)}(n, l)$ coefficients.

During the minimum, the total average area of the spots is a few times lower than during the maximum. It is also narrower, such as the integral in equation (14) is small, reducing $a_j^{(AR)}(n, l) \simeq 0$. During the phase of minimum of activity, the activity can effectively be considered as nonexistent (see Section 5 for the analysis on solar data), so that $a_2(n, l)$ is dominated by the centrifugal term $a_2^{(CF)}(n, l)$ and the other even a-coefficients are null.

The overall latitudinal profile is seemingly following a bell-shape with sharp slopes during periods of activity. Figure 2c compares data between 1986 and 2016 with three models for the active latitudes: a model using the gate function $F(\theta|X) = \Pi(\theta_0, \delta)$, a triangular function $\Lambda(\theta_0, \delta)$ and

282 a Gaussian function $\mathcal{N}(\theta_0, \delta)$. The parameters of these were adjusted manually to approximately
 283 match the solar spot active latitudes profile. The triangular and the Gaussian functions describe
 284 equivalently the data, while the gate function initially proposed by Gizon (2002) is roughly fitting
 285 the data. Because spots are strictly appearing at latitudes below 45° , the Λ function may be the most
 286 suitable for the Sun. Nevertheless, these three functions are retained and compared herefurther.

287 *3.3. Assumptions on the a-coefficients*

288 The most direct method for measuring the asphericity is to evaluate it directly for each mode (n,l) ,
 289 that is, measuring the terms $a_j(n, l)$. This being already difficult for low-order a-coefficients of
 290 the Sun (Chaplin et al. 2003), it seems unreasonable to expect an accurate measurement of all
 291 individual $a_j(n, l)$ using asteroseismic data. These have a lower signal-to-noise ratio and severely
 292 reduced visibility at $l \geq 3$ due to the integrated photometry. After a trial and error process, jointly
 293 with power spectra simulations, we could identify a set of assumptions ensuring reliable and precise
 294 measurement of a-coefficients.

295 We first consider a fictitious star rotating as a solid-body with a solar activity level ($\epsilon_{nl} \simeq$
 296 5×10^{-4} , Gizon (2002)) with $a_1 = 1000$ nHz. The observed oscillation frequencies of 16 Cyg
 297 A are used here (Davies et al. 2015; Kamiaka et al. 2018). Split frequencies are derived using
 298 equations (1), (7), (13), (14), and converted into a-coefficients using equations (A.8-A.19). The a-
 299 coefficients are linear functions of the frequency, which is expected as $F(\theta|\theta_0, \delta)$ describes a single
 300 active region. Thus, a reasonable assumption is to consider those as pure first order polynomial
 301 functions of frequencies. However, tests on artificial spectra showed that it is often difficult to
 302 evaluate the slope of the a-coefficients. This is because the uncertainty on any a_j is at least of the
 303 same order as its variations within the range of observed frequencies. This suggests that current
 304 asteroseismic data lack the resolution and the signal-to-noise to reliably measure the frequency
 305 dependence on the a-coefficients.

306 Figure 3 shows $a_2^{(AR)}$, $a_4^{(AR)}$, $a_6^{(AR)}$ for activity described by $F = \Pi$ (black) or Λ (red) or \mathcal{N}
 307 (blue). These are the mean coefficients for the fictitious active star, as a function of θ_0 and δ .
 308 The figure indicates that there is a simple relationship between the a-coefficients, the co-latitude
 309 θ_0 and the extension of the activity zone δ , independently of the shape of activity. In the case
 310 of $F = \Pi$, the lines are cut near the pole and the equator due to the condition $\theta_0 \geq \delta/2$ and
 311 $\theta_0 \leq \pi - \delta/2$. In the other profiles, edges effects (truncation) has noticeable effects near the equator.
 312 The definition of δ differs between the three profiles, which explains that a factor of a few in $a_j^{(AR)}$
 313 is noticeable between $F = \Pi$, Λ and \mathcal{N} for a given δ . Note that adding the centrifugal effect reduces
 314 $a_2(n, l) = a_2^{(AR)}(n, l) + a_2^{(CF)}(n, l)$, because the coefficient $a_2^{(CF)}(n, l)$ is always negative.

315 If an observation can constrain only a single a-coefficient (e.g. a_2), there often exists a degen-
 316 eracy in θ_0 as multiple value of a_j can be obtained for a given θ_0 . As the figure shows, measuring
 317 two a-coefficients alleviates this degeneracy, provided that uncertainties are small enough. In other
 318 words, the accuracy on the inference of the active region using a-coefficients is ensured only if we

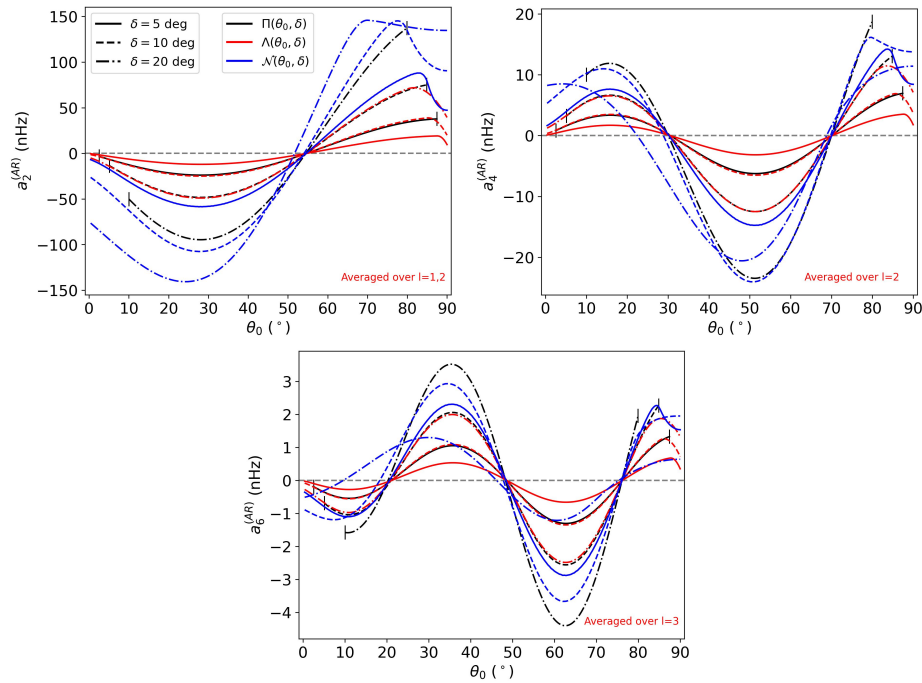


Fig. 3. Average $a_j^{(AR)}$ (no centrifugal effect accounted for) with $\epsilon_{nl} = 5.10^{-4}$ in function of θ and δ and for the gate (Π), triangle (Λ) and gaussian (\mathcal{N}) filter functions. Uniqueness is guaranteed for θ only if at least two a-coefficients are measured.

can simultaneously constrain two a-coefficients (e.g. a_2 and a_4). This is essential to distinguish an activity near the pole ($\theta_0 \lesssim 30^\circ$) from mid-latitude ($30^\circ \lesssim \theta_0 \lesssim 60^\circ$) or from near the equator ($\theta_0 \gtrsim 60^\circ$). 319
320
321

It indicates that the loss of information resulting from the averaging does not affect the accuracy³. Figure 3 also indicates that for a star with an activity intensity and an activity zone of extension comensurate with the one of the Sun ($\epsilon_{nl} \simeq 5.10^{-4}$, $\delta \simeq 10^\circ$ when $F = \Pi$), the uncertainty on $a_2^{(AR)}$ must be approximately $\lesssim 25$ nHz, the one for $a_4^{(AR)} \lesssim 10$ nHz and $a_6^{(AR)} \lesssim 1.5$ nHz to be able to detect significant departures of the coefficients. This is to be compared with the spectral resolution of 7-14nHz for 2-4 years of observation, typical of the longest Kepler observations. In the Figure 3, $a_2^{(AR)}$ is obtained by averaging $l = 1, 2$, $a_4^{(AR)}$ by averaging $l = 2$, while $a_6^{(AR)}$ is only constrained by $l = 3$ modes. Averaging $a_2^{(AR)}$ and $a_4^{(AR)}$ over $l = 1, 2, 3$ increases the maximum range of the a-coefficients by a factor ≈ 1.5 for $a_2^{(AR)}$ and ≈ 2 for $a_4^{(AR)}$, respectively, without changing the overall shape of the function. In Sun-like stars, the $l = 3$ modes have a HNR at least ten times lower than $l = 0$ modes because the height ratio between $l = 3$ and $l = 0$ modes is around 0.08 for the Sun (Toutain & Gouttebroze 1993; Toutain et al. 1998). These modes are therefore difficult to observe. Due to all of the above, it is extremely challenging to measure a_6 with current existing data. In the following, we will thus focus on assessing the reliability domains of a_2 and a_4 only. 322
323
324
325
326
327
328
329
330
331
332
333
334
335

³It does however increase the uncertainty by a factor of a few.

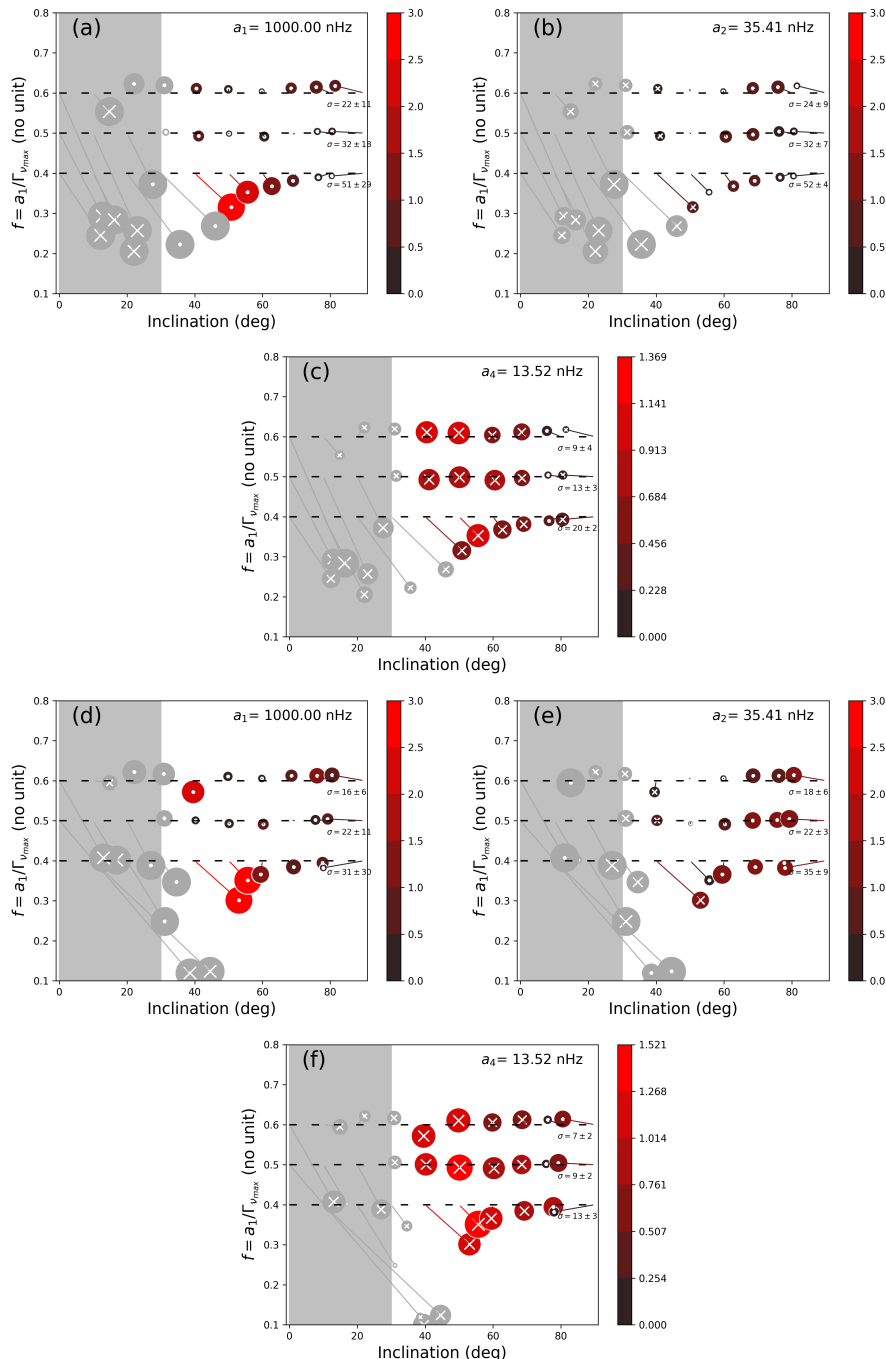


Fig. 4. Bias analysis for $\widehat{HNR} = 30$ for an equatorial activity band ($\theta_0 = 85^\circ, \delta = 10^\circ$) of similar intensity to the Sun ($\epsilon_{nl} = 5 \times 10^{-4}$), for $T_{obs} = 2$ years (top) and $T_{obs} = 4$ years (bottom). Color and size of the circles indicate the modulus of the bias. **The color bar gives its scale normalised by the uncertainty, $b(a_j)/\sigma$.** A white cross is for an underestimation. A white dot is for an overestimation. Below 30° of inclination (gray area and symbols), the results are not reliable.

336 4. Bias analysis on a_1 a_2 and a_4

337 In order to understand the reliability of the inference on low-degree a-coefficient, it is necessary to
 338 perform a bias analysis. This requires to fit an ensemble of emulated spectra that are representative
 339 of Sun-like stars and to compare the results with the true inputs.

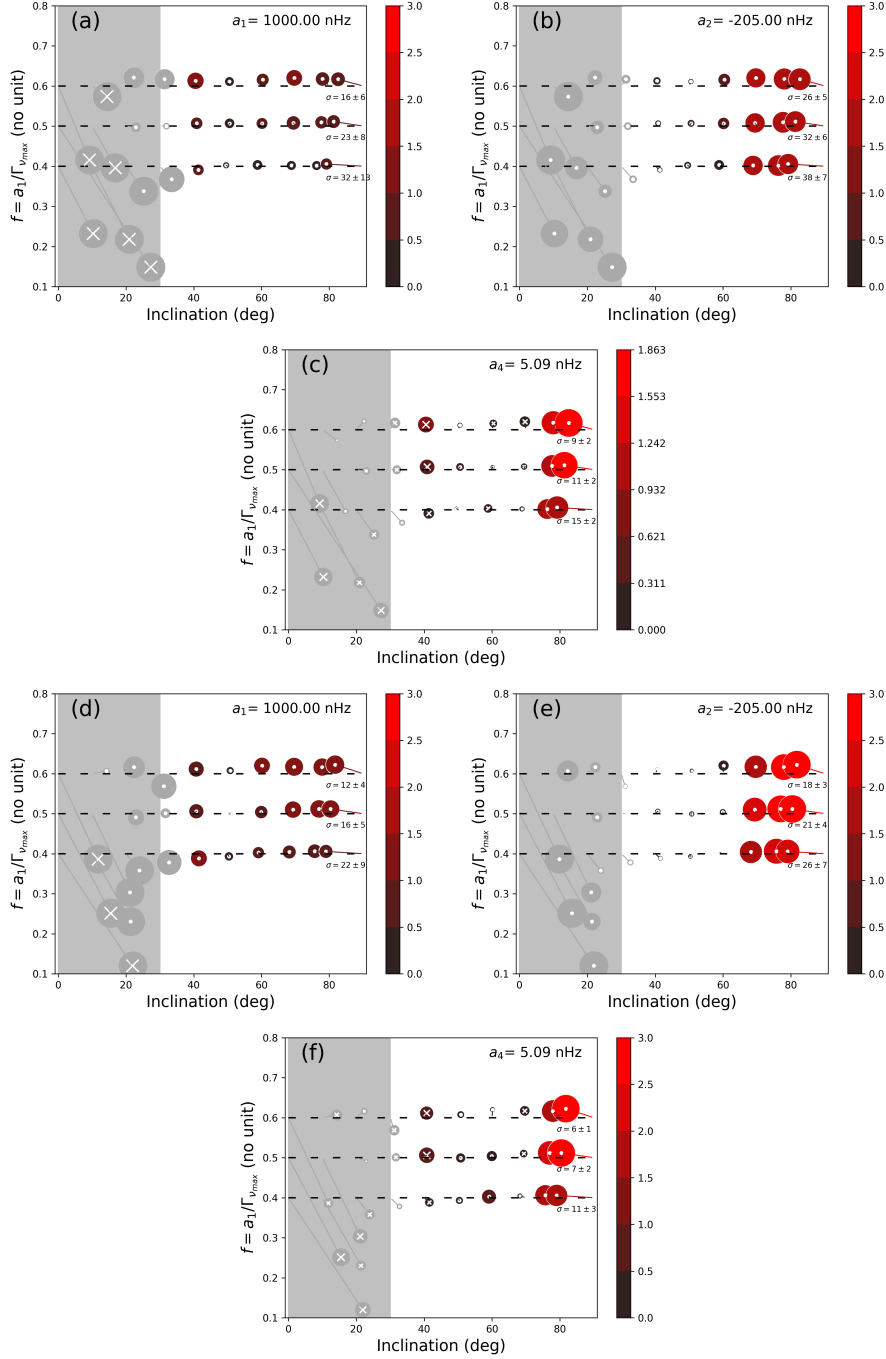


Fig. 5. Bias analysis for $\widehat{HNR} = 30$ for a large polar activity cap ($\theta_0 = 22.5, \delta = 45$) of similar intensity to the Sun ($\epsilon_{nl} = 5.10^{-4}$), for $T_{obs} = 2$ years (top) and $T_{obs} = 4$ years (bottom).

4.1. Test setup

340

The synthetic spectra use the frequencies, heights, widths and the noise background profile of 16 Cyg A as a template for the simulations. We want to specifically study the impact of the mode blending (effect of $a_1/\Gamma_{\nu_{max}}$), the stellar inclination (i), observation duration (T_{obs}) and of the maximum Height-to-Noise background (\widehat{HNR}) on the accuracy of a_1 , a_2 and a_4 . Grids of spectra are built in the case of an equatorial band of activity and of a large polar activity. The grid parameters and their ranges are provided in Table 4.1 and discussed further below. The spectra are made using

341

342

343

344

345

346

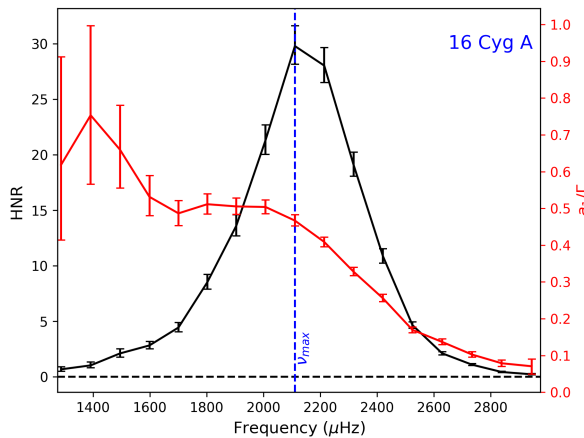


Fig. 6. HNR (black) and a_1/Γ ratio (red) for 16 Cyg A, which is the reference star used to make simulations.

347 a spectrum simulator code⁴ that take the reference star (or template) and modify its properties to
 348 match the requirement of the user. The template is altered in terms of HNR following a similar
 349 approach as in Kamiaka et al. (2018). The main difference is that we considered a frequency-
 350 dependent noise background. Heights are rescaled according to,

$$H_{n,l=0} = \frac{\widehat{HNR}}{\widehat{HNR}_{\text{ref}}} H_{\text{ref}}(n, l=0) \quad (17)$$

351 where \widehat{HNR} is the maximum HNR of the synthetic star, $\widehat{HNR}_{\text{ref}}$ the maximum HNR of the reference
 352 star and $H_{\text{ref}}(n, l=0)$ the $l=0$ heights of the reference star.

353 As for the mode blending factor $f = a_1/\Gamma_{\nu_{\text{max}}}$, it is calculated fixing a_1 and altering $\Gamma_{\nu_{\text{max}}}$ such
 354 that,

$$\Gamma_{\nu_{\text{max}}} = \frac{a_1}{f}. \quad (18)$$

355 A fiducial value of $a_1 = 1000 \text{ nHz}$ ($\simeq 2.4$ the solar rotation) is used in the simulation. Note that this
 356 differs from Kamiaka et al. (2018) where the splitting was modified in order to obtain the desired
 357 mode blending factor.

358 As shown in Table 4.1, three HNR cases are investigated, ranging from 10 to 30. Two ob-
 359 servation durations are considered: 2 years and 4 years. This is representative of the best Kepler
 360 observations (Davies et al. 2015) and of future observations from PLATO (Rauer et al. 2014).
 361 Similarly to the test cases of Gizon (2002), a_2 and a_4 are determined for an equatorial activity of
 362 extension of the same order as in the Solar case ($\delta \simeq 10^\circ$), and in the case of a large polar cap
 363 ($\delta = 45^\circ$). Both situations assume an activity of the same order as for the Sun. The priors are set
 364 in a similar manner as they would if the power spectrum was from a real star. The evaluation of
 365 the mode parameters is performed using a MCMC method, like for actual stars (see Appendix B
 366 for further details), but on the limit-spectrum (no noise). Fitting the limit spectrum allows to **assess**

⁴The tool suite used here along with the data inputs/outputs are available at https://github.com/OthmanB/Benomar2022/tree/version_2.

Variable	Values		
HNR	10, 20, 30		
T_{obs} (years)	2, 4		
$a_1/\Gamma_{v_{\max}}$	0.4, 0.5, 0.6		
ϵ_{nl}	$5 \cdot 10^{-4}$		
a_1 (nHz)	1000		
Act. Region	$\theta_0 = 85^\circ, \delta = 10^\circ$ (Eq.)	$\theta_0 = 22.5^\circ, \delta = 45^\circ$ (Pol.)	
a_2 (nHz)	35.41	-205.06	
a_4 (nHz)	13.52	5.09	

Table 1. Parameters set to construct artificial power spectra. a_2 and a_4 are determined assuming active regions located either in an equatorial band or in a polar cap.

	Active Sun	Quiet Sun	16 Cyg A	16 Cyg B
\widehat{HNR}	100	70	30	29
$\Delta\nu$ (nHz)	135.1	135.1	103.35	116.92
a_1 (nHz)	421 ± 10	410 ± 9	614 ± 37	607 ± 78
a_1/Γ	0.45 ± 0.03	0.40 ± 0.02	0.45 ± 0.04	0.58 ± 0.1
inclination ($^\circ$)	90 (fixed)	90 (fixed)	45 ± 4	35 ± 3
a_2 (nHz)	80 ± 19	11 ± 21	19.6 ± 8.6	18.5 ± 23.5
a_4 (nHz)	5.0 ± 10.5	2.1 ± 9.8	2.9 ± 8.9	-27.9 ± 6.5 or -1.0 ± 6.7
$a_2^{(\text{CF})}$ (nHz)	-6.5 ± 0.3	-6.1 ± 0.3	-17.0 ± 2.2	-15.5 ± 4.0
$a_2^{(\text{AR})}$ (nHz)	86.2 ± 18.7	16.7 ± 20.4	39.0 ± 20.6	34.0 ± 21.8
$b(a_2)$ (nHz)	/	/	-10	-10
$b(a_4)$ (nHz)	/	/	-10	-10

Table 2. Summary of the main parameters for the Sun and 16 Cyg A and B used to infer the activity. fiducial biases $b(a_2)$ and $b(a_4)$ for 16 Cyg A and B are set after inspection of Figure 4. The lowest (highest) solution of a_4 for 16 Cyg B is has a probability of 30% (70%).

the systematic errors by calculating the expectation value of the probability density function. The 367
expected uncertainty can also be known by computing the standard deviation. 368

4.2. Results

 369

To appreciate the level of inaccuracy achieved when measuring $a_j, j \in [1, 2, 4]$ coefficients, the bias 370
is calculated for $a_j, f = a_1/\Gamma_{v_{\max}}$ and i , 371

$$\begin{aligned} b(a_j) &= E[a_j^{\text{meas}}] - a_j^{\text{true}}, \\ b(F) &= E[F^{\text{meas}}] - F^{\text{true}}, \\ b(i) &= E[i^{\text{meas}}] - i^{\text{true}}. \end{aligned} \quad (19)$$

Here, the letter E refers to the expectation value (median) from the probability density function. 372

Figure 4 shows the resulting bias maps for a-coefficients as a function of the blending factor F 373
and of the stellar inclination for a-coefficients corresponding to an equatorial activity band. Figure 5 374
is the same but for a large polar activity cap. The bias is represented as a projected three dimensional 375
vector using the three quantities defined by equation (19) and for $j \in [1, 2, 4]$. To evaluate the 376
importance of the bias on a_j , the plot shows $b(a_j)/\langle \sigma_{a_j}(i, F) \rangle_i$, with $\langle \sigma_{a_j}(i, F) \rangle_i$ the average standard 377
deviation of the probability density functions obtained by the MCMC sampling over $i \in [30^\circ, 90^\circ]$. 378
The value of $\langle \sigma_{a_j}(i, F) \rangle_i$ (noted σ for convenience hereafter) and its variance along the inclination 379

axis is also shown on the plots. A value of $b(a_j)/\sigma$ greater than one indicates that the inaccuracy exceeds the typical expected uncertainty at 1σ and may lead to significantly biased results during the subsequent analyses of the a-coefficients. A negative bias (underestimation) for a_j is indicated by a cross within the circle while a positive bias (overestimation) by a dot. The darker the color, the smaller the norm of the normalised bias. The size of the circle symbols is also proportional to the bias, but capped to 3, to avoid excessively large symbols when $i < 30^\circ$ (see next paragraph for explanations). The case of observations of duration of 2 years are in the top figures (a, b, c) while the 4 years observation case is shown in bottom figures (d, e, f).

We first note that the biases on inclination and on F are consistent with results from Kamiaka et al. (2018). Regions of stellar inclination below 30° are found to provide very unreliable results and the median of the inclination is biased toward $\simeq 80^\circ$ when the true input is $i = 90^\circ$. Meanwhile, biases in a_1 are found to often exceed 50% in the gray area⁵, indicating that for inclination below $\simeq 30^\circ$, the median estimator of the probability density function might not be trusted. This justifies also the range for the calculation of σ . In the following we therefore focus the discussion of the figures for the region above 30° .

In the case of an equatorial zone of activity, we note that measurements of a_1 may have negligible inaccuracies when the blending factor F is above 0.4, but starts to be significantly deteriorated at (and probably below) $f = 0.4$ because $|b(a_1)|/\sigma$ exceeds 1.5 when $i < 50^\circ$. Split components are then overlapping significantly leading to important degeneracies between a-coefficients, mode widths and the stellar inclination. Meanwhile, we note that the biases on a_2 and a_4 remain mild compared to the uncertainty ($|b(a_2)|/\sigma < 1$ and $|b(a_4)|/\sigma < 1$), even for $f = 0.4$.

In the case of a polar active region, $|a_2|$ represents $\simeq 20\%$ of the a_1 coefficient. In these conditions, we note that $b(a_1)/\sigma$ does not exceed the unity (see (a) and (d)), indicating a good accuracy. The terms $|b(a_2)|/\sigma$ and $|b(a_4)|/\sigma$ are also lower than 0.5, provided that the stellar inclination is between 30° and 70° . This indicates that a large a_2 coefficient is generally associated with a higher accuracy for all a-coefficients. The plot also demonstrates that a large zone in the parameter space has moderate to small bias.

Interestingly, figures for \widehat{HNR} of 10 and 20 (Figures D.1-D.4 in Appendix D) lead to similar conclusions. Therefore, even in less favorable \widehat{HNR} conditions, the expected uncertainty on the measurement generally encompass the bias provided that the stellar inclination exceeds $\simeq 30^\circ$ (ensuring that $m \neq 0$ have significant amplitudes) and that the mode blending factor is above 0.4. This indicates that for a majority of stars observed by Kepler, the accuracy may not be a major issue when measuring a_1 , a_2 and a_4 and provided that a carefull assesment of F and i is performed. Note however that the average uncertainty σ does usually increase when the \widehat{HNR} and/or the observation duration decrease, which will have an impact on the precision of the determination of the active region.

⁵This is likely due to the fit mis-identifying the $l = 2, m = \pm 1$ with $l = 2, m = \pm 2$, effectively doubling or halving the a_1 coefficient.

	Active Sun	Quiet Sun	16 Cyg A		16 Cyg B			
	.	.	No bias	bias corr.	$a_4 \approx -27.9$	$a_4 \approx -1.0$	$a_4 \approx -27.9$	bias corr.
$\ln(P(\mathbf{O} \mathbf{M}_{CF})$	-10.809	-0.367	-1.856	-3.889	-10.596	-1.228	-5.910	-2.951
$\Pi(\theta_0, \delta)$	$\epsilon_{nl} (10^{-4})$	$7.6^{+25.5}_{-5.3}$	$3.7^{+19.6}_{-3.1}$	$5.3^{+19.6}_{-4.1}$	$6.4^{+24.8}_{-4.8}$	$12.5^{+31.9}_{-7.5}$	$4.6^{+20.8}_{-3.7}$	$11.5^{+39.4}_{-7.9}$
	θ_0 (deg)	76^{+8}_{-7}	60^{+19}_{-41}	71^{+13}_{-14}	79^{+8}_{-10}	58^{+3}_{-3}	67^{+14}_{-25}	61^{+3}_{-4}
	δ (deg)	7^{+16}_{-5}	2^{+11}_{-2}	4^{+16}_{-3}	5^{+15}_{-4}	8^{+7}_{-6}	3^{+13}_{-2}	$6^{+14.8}_{-4.6}$
$\ln(P(\mathbf{O} \mathbf{M}_{AR})$	-0.685	-0.347	-0.482	-0.656	-0.878	-0.449	-0.781	-0.611
Significance (%)	> 99.99	50.5	79.8	96.2	> 99.9	68.6	99.3	91.2
$\Lambda(\theta_0, \delta)$	$\epsilon_{nl} (10^{-4})$	$14.2^{+33.0}_{-9.8}$	$17^{+42.9}_{-14.2}$	$15.4^{+39.5}_{-12.2}$	$13.6^{+34.1}_{-4.8}$	$21.1^{+35.2}_{-12.6}$	$15.1^{+38.9}_{-12.4}$	$17.3^{+34.0}_{-11.4}$
	θ_0 (deg)	76^{+9}_{-7}	49^{+27}_{-36}	66^{+16}_{-41}	78^{+9}_{-21}	58^{+2}_{-3}	58^{+21}_{-40}	61^{+3}_{-4}
	δ (deg)	7^{+16}_{-5}	6^{+19}_{-5}	6^{+17}_{-4}	5^{+15}_{-4}	10^{+16}_{-6}	6^{+17}_{-5}	8^{+16}_{-5}
$\ln(P(\mathbf{O} \mathbf{M}_{AR})$	-0.698	-0.296	-0.492	-0.699	-0.930	-0.427	-0.847	-0.639
Significance (%)	> 99.99	51.8	79.6	96.0	> 99.99	69.0	99.4	91.0
$\mathcal{N}(\theta_0, \delta)$	$\epsilon_{nl} (10^{-4})$	$3.7^{+16.0}_{-2.2}$	$15.1^{+42.8}_{-13.5}$	$12.2^{+39.5}_{-10.5}$	$6.6^{+24.3}_{-5.9}$	$13.3^{+24.1}_{-7.0}$	$12.6^{+41.0}_{-11.0}$	$6.6^{+24.3}_{-5.5}$
	θ_0 (deg)	73^{+11}_{-10}	48^{+28}_{-34}	63^{+18}_{-38}	75^{+11}_{-27}	56.6^{+3}_{-7}	55^{+23}_{-37}	75^{+11}_{-27}
	δ (deg)	$9^{+26.6}_{-8}$	7^{+20}_{-6}	6^{+22}_{-5}	4^{+20}_{-3}	6^{+22}_{-5}	7^{+21}_{-6}	4^{+20}_{-3}
$\ln(P(\mathbf{O} \mathbf{M}_{AR})$	-0.708	-0.384	-0.584	-0.811	-0.943	-0.516	-0.811	-0.759
Significance (%)	> 99.99	49.6	78.1	95.6	> 99.99	67.1	99.4	90.0
Average	$\epsilon_{nl} (10^{-4})$	$7.7^{+25.7}_{-5.6}$	$11.4^{+41.6}_{-10.0}$	$9.2^{+34.2}_{-7.5}$	$8.0^{+29.4}_{-6}$	$15.5^{+30.7}_{-9.1}$	$10.5^{+37.2}_{-9.0}$	$11.8^{+31.5}_{-7.5}$
	θ_0 (deg)	75^{+10}_{-8}	53^{+25}_{-37}	68^{+14}_{-14}	78^{+9}_{-14}	58^{+3}_{-4}	61^{+18}_{-34}	60^{+4}_{-6}
	δ (deg)	7^{+22}_{-6}	5^{+18}_{-4}	5^{+18}_{-4}	5^{+17}_{-4}	8^{+18}_{-6}	6^{+18}_{-5}	7^{+19}_{-6}
$\ln(P(\mathbf{O} \mathbf{M}_{AR})$	-0.697	-0.342	-0.519	-0.722	-0.917	-0.464	-0.824	-0.670
Significance (%)	> 99.99	50.6	79.2	96.0	> 99.99	68.2	99.4	90.7

Table 3. Statistical summary for the activity parameters and their model log-marginal likelihood $\ln(P(\mathbf{O}|\mathbf{M}_{AR})$) when $F(\theta|\mathbf{x}) = \Pi(\theta_0, \delta)$, $\Lambda(\theta_0, \delta)$ or $\mathcal{N}(\theta_0, \delta)$. $\ln(P(\mathbf{O}|\mathbf{M}_{CF})$ is the log-marginal likelihood for a pure centrifugal effect. The Activity significance is the probability that the activity is necessary to explain the data and derived from the log-marginal likelihoods. Uncertainty on the activity significance is less than 0.25%.

5. Analysis of solar data

416

The Sun has a well-known 11-year activity cycle that makes it ideal for testing further the accuracy 417
of the method. The Sun activity cycle is analysed at two instants, highlighted in Figure 2 and for 418
which high-quality **helioseismic** data are available: (a) the maximum of activity between January 419
1999 and January 2002; and (b) the minimum of activity between January 2006 and January 2009. 420
Data are from the Variability of Solar Irradiance and Gravity Oscillations instrument aboard SOHO 421
spacecraft (Frohlich et al. 1997) and presents very few gaps. 422

5.1. a-coefficients of the Sun

423

As for the simulated data, the analysis consists in fitting the power spectrum for cases (a) and (b), 424
to measure the a_1 , a_2 and a_4 coefficients using the bayesian modeling and the MCMC method 425
described in the Appendix B. Figures of the best fits and their discussions are provided in Appendix 426
E. The goal being to evaluate the accuracy of the inference of the activity zone from a-coefficients, 427
the presented results are for a stellar inclination fixed to 90° , instead of having it as a free parameter. 428
This value correspond approximately to the stellar inclination as seen by the SOHO satellite. This 429
alleviates biases on a_j coefficients that may arise due to the systematic underestimation of i when 430

431 it is close to 90 degrees. However, carried tests with a free inclination during the maximum of
 432 activity⁶ lead to a difference of -12nHz in a_2 and to -1.3nHz in a_4 . This is consistent with the
 433 expected difference from the bias map of Figure 4. In agreement with the discussion of Section 4,
 434 the difference does not have a significant impact on the activity inference because the uncertainties
 435 for those parameters are larger than the observed measurement shift.

436 Figure 7 shows the measured probability distribution function of the relevant parameters along
 437 with their correlations during the maximum of solar activity (left) and the minimum (right). The
 438 $a_2^{(CF)}$ distribution in red represents the expected centrifugal effect on a_2 as derived from frequency
 439 shifts $\delta_{nlm}^{(CF)}$ of equation (13). The distributions are Gaussians and show a weak correlation, reflecting
 440 the quality of the data. Between the maximum and the **minimum** of activity, the a_2 coefficient
 441 drifted significantly, from $a_2 = 80 \pm 19 \text{nHz}$ to $a_2 = 11 \pm 21$ falling within the 1σ confidence
 442 interval of the centrifugal term. Although a_4 may have changed, the effect is below uncertainty
 443 levels and remain close to 0. As shown in Figure 15, other time intervals may lead to a_4 departing
 444 from 0. The figures demonstrate that a comparison of a_2 and $a_2^{(CF)}$ may reveal the activity of a Sun-
 445 like star. At the maximum of activity $a_2^{(CF)}$ is inconsistent with a_2 at 4.5σ , but it is in agreement at
 446 1σ during the mimimum of activity. Interestingly, Chaplin et al. (2003) also studied in details the
 447 frequency asymmetry of $l = 2$ modes using BiSON and GOLF data with a different methodology,
 448 and over period that encompasses the maximum of 1999-2002. Their measure consider only T_{n22}
 449 so a direct comparison is not straightforward. However, we note that with a 844 day-long timeseries
 450 starting in Feb 1999⁷, they detect a frequency shift $T_{n22} \simeq 190 \text{nHz}$ at a similar significance ($\simeq 4\sigma$)
 451 than us when averaging over all modes between $\simeq 2000 - 3300 \mu\text{Hz}$ (to be compared to our range
 452 of $\simeq 2300 - 3600 \mu\text{Hz}$). Their Figure 8 also show that the global effect of the activity cycle between
 453 1994 and 2000 is evident on the averaged T_{n22} while the frequency dependence of T_{n22} may have
 454 too large uncertainties to ascertain a frequency-trend. This is in line with our own findings (see our
 455 Section 3.3).

456 A rigorous statistical evaluation of our significance requires the joint use of a_2 and a_4 . This is
 457 discussed in Section 5.2, along with other activity results. Finaly note that for inclination of $\simeq 90$
 458 degrees, it is not possible to determine a_3 , because the amplitudes of the azimuthal components for
 459 $l = 1, 2$, are not favorable (Gizon & Solanki 2004).

460 5.2. Activity of the Sun

461 The activity intensity and its latitudinal coverage is derived from a fit of the $a_2^{(AR)}$ and $a_4^{(AR)}$ coef-
 462 ficients. Technical details are in Appendix C. Statistical summary of the results are listed in Table
 463 3. The statistical significance of the activity exceeds 99.99% (highly significant) at the maximum
 464 of activity, but is around 50.6% (not significant) during the minimum of activity, demonstrating
 465 the possibility of detecting activity in Sun-like stars. The choice of the function F describing the
 466 active region changes the detection significance by only a few percents. The three explored models

⁶The measured stellar inclination is $i = 74 \pm 3$ degrees at the maximum of activity of 1999-2002.

⁷To be compared to our timeserie of 1095 days starting in Jan 1999.

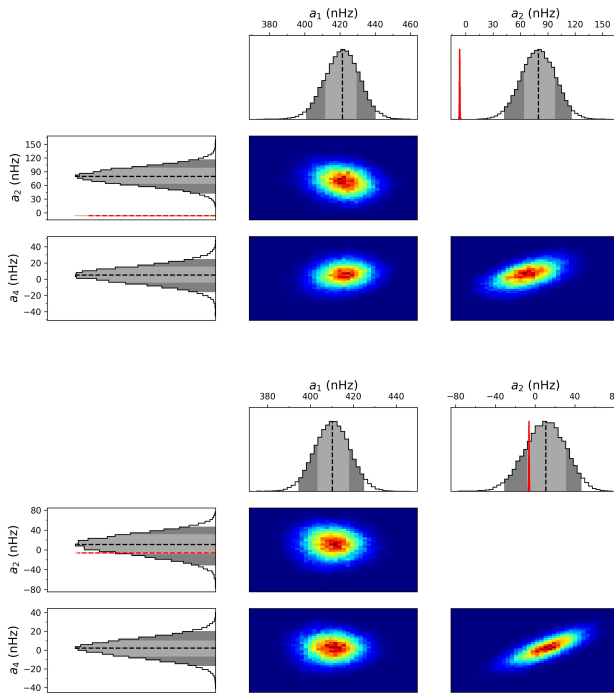


Fig. 7. Probability Density Functions and their correlations, obtained by MCMC for coefficients a_1, a_2, a_3, a_4 for the Sun at Maximum of activity (1999-2002, left) and at minimum of activity (2006-2009, right). The red curve is the expected a_2^{CF} coefficient for a pure centrifugal distortion. The light and dark gray PDF filling is for the 1σ and 2σ confidence interval, respectively.

fit equivalently the data implying that the shape of the active region cannot be determined with 467 currently available a_2 and a_4 constraints. 468

Figure 8 and 9 show $\epsilon_{nl} = \epsilon, \theta_0$ and δ for the Sun at its maximum of activity (1999-2002) and 469 its minimum (2006-2009), respectively. There is no major differences between the three activity 470 profiles, although it is noted that uncertainties are larger in the case of a triangular and a Gaussian 471 activity zone. During the maximum of activity, $\epsilon \approx 0$ is clearly excluded (see inset). With $F = \Pi$, 472 we observe a log-normal distribution, with median $7.6 \cdot 10^{-4}$, consistent with the value reported by 473 Gizon (2002). However, the uncertainty is large, suggesting that only the order of magnitude can 474 be constrained in Sun-like stars. At the minimum of activity, the log-normal distribution morphs 475 into a $1/x$ law, similar to the Jeffreys prior. This is a sign of weaker statistical significance for the 476 activity. 477

The co-latitude $\theta_0 \approx 75^\circ$ is consistent with the butterfly diagram, which suggests $\theta_0 \approx 80^\circ$. At 478 the minimum of activity and despite a non-significant detection, the probability distribution of θ_0 479 shows a weak indication of activity at mid and high co-latitudes. Despite the high significance of 480 the detection during the maximum of activity, δ is poorly constrained, showing that this parameter 481 is challenging to measure on the Sun and on other Sun-like stars. 482

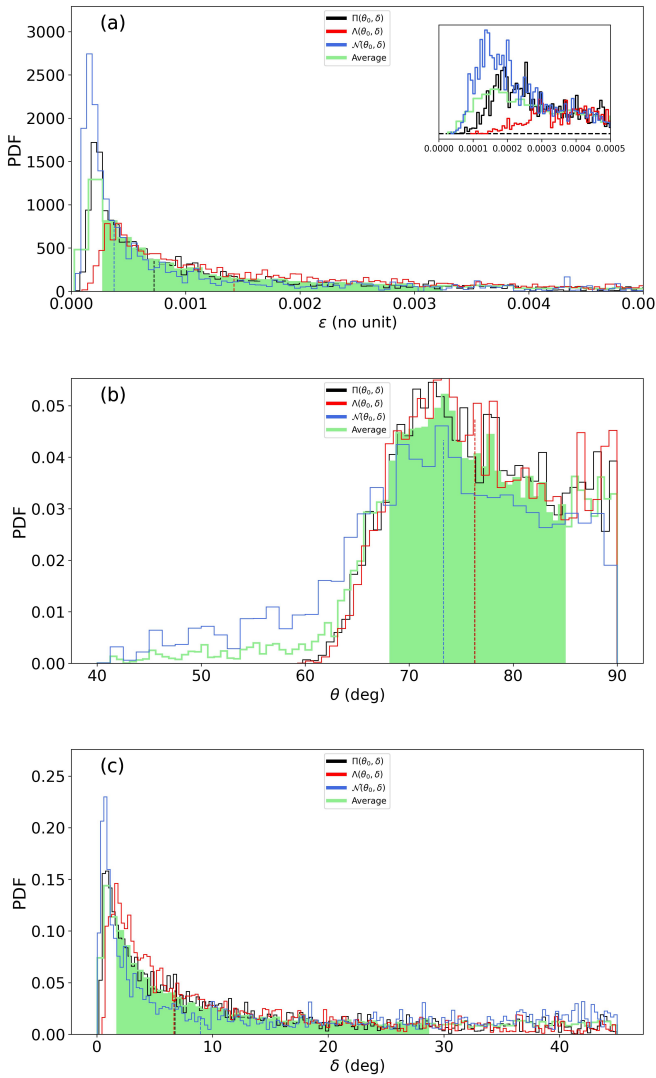


Fig. 8. Inferred pdf for (a) ϵ , (b) θ_0 and (c) δ , during the Sun maximum activity of 1999-2002. The inset of (a) is a zoom into the near-zero ϵ values with smaller binning.

483 6. Analysis of 16 Cyg A and B

484 Due to their brightness (magnitudes $V=5.95$ and 6.20) 16 Cyg A and B have modes with the highest
 485 HNR among all of Sun-like stars observed asteroseismically so far. They constitute ideal candidates
 486 to evaluate the activity. The two stars are wide binaries, with a confirmed planet around 16 Cyg B
 487 (Cochran et al. 1997) and were extensively studied (e.g. Neckel 1986; King et al. 1997; Deliyannis
 488 et al. 2000; Schuler et al. 2011; Takeda 2005; Metcalfe et al. 2012; Lund et al. 2014; Verma et al.
 489 2014; Buldgen et al. 2015; Deal et al. 2015; Metcalfe et al. 2016; Roxburgh 2017; Bellinger et al.
 490 2017; Maia et al. 2019; Bazot et al. 2019; Bazot 2020; Farnir et al. 2020; Morel et al. 2021; Buldgen
 491 et al. 2022; Nsamba et al. 2022). The 2.5 years (13 September 2010 to 8 March 2013) observation
 492 by the Kepler space-borne instrument is used in this section to measure pulsation parameters. The
 493 data are the same as those used in Bazot et al. (2019) for which instrumental issues (outliers, jumps,
 494 trends) and the quarter stitching is performed using the procedure described in García et al. (2011a).
 495 The binary system has precisely measured angular diameters, making it two of the few Sun-like

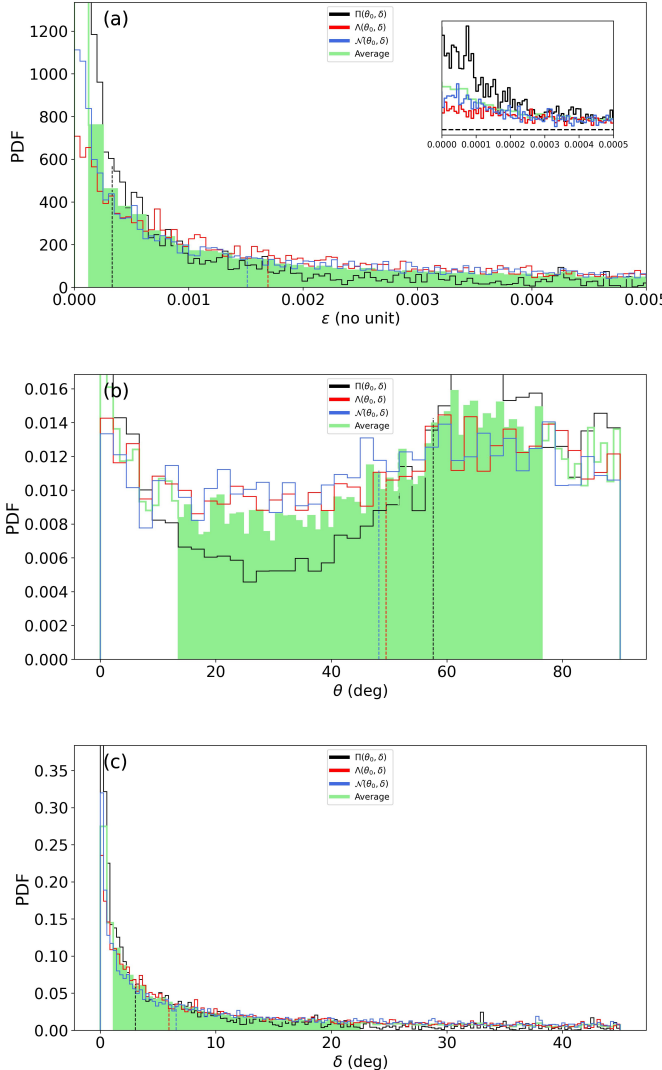


Fig. 9. Inferred pdf for (a) ϵ , (b) θ_0 and (c) δ , during the Sun minimum activity of 2006-2009. The inset of (a) is a zoom into the near-zero ϵ values with smaller binning.

stars with known interferometric radii. Their measured radius are $1.22 \pm 0.02R$ and $1.12 \pm 0.02R$ for 496
16 Cyg A and B, respectively (White et al. 2013). Their spectroscopic parameters are very close to 497
those of the Sun: Their effective temperatures are $T_{\text{eff}} = 5825 \pm 50$ K, $T_{\text{eff}} = 5750 \pm 50$ K and their 498
metallicity are $[M/H] = 0.10 \pm 0.09$, $[M/H] = 0.05 \pm 0.06$ (Ramírez et al. 2009) for 16 Cyg A and 499
B, respectively. With an estimated age of around 7 Gyrs for both stars (Metcalfe et al. 2016; Bazot 500
2020, e.g.), they are significantly older than the Sun. 501

6.1. Seismic constraints for 16 Cyg A

Earlier studies of 16 Cyg A revealed around 60 modes of pulsations with significance in the power 503
spectrum⁸. The asteroseismic analysis of Davies et al. (2015) found a stellar inclination of 56^{+6}_{-5} 504
and a rotation $23.8^{+1.5}_{-1.8}$ ($\langle \delta\nu_{nlm}/m \rangle_{nl} \simeq 486^{+40}_{-29}$ nHz). Using a refined power spectrum modeling that 505

⁸The exact value may differ from author to author, due to different choice for the significance.

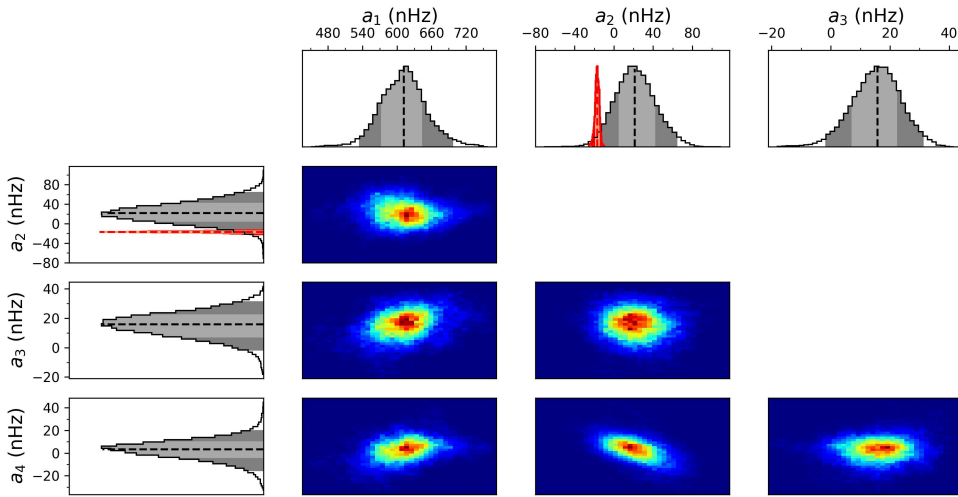


Fig. 10. Probability Density Functions and their correlations, obtained by MCMC of the power spectrum of 16 Cyg A and for coefficients a_1, a_2, a_3, a_4 for 16 Cyg A. The red curve shows the expected $a_2^{(CF)}$ coefficient for a pure centrifugal distortion of the star. The light and dark gray PDF filling is for the 1σ and 2σ confidence interval, respectively.

506 account for a_1, a_3 and parametrises the cavity asphericity $(R_{\text{eq}} - R_{\text{pol}})/R_{\text{eq}}$, Bazot et al. (2019)
 507 reported values ($i = 58.5 \pm 6.8, a_1 = 464 \pm 43\text{nHz}$), consistent with Davies et al. (2015).

508 Figure 10 shows the probability density function for a_1, a_2, a_3 and a_4 for 16 Cyg A, along with
 509 their correlation and with $a_2^{(CF)}$ superimposed in the a_2 quadrant. Table 2 synthetizes the inferred val-
 510 ues of the coefficients. The probability density functions are near-Gaussian and thus the quadratic
 511 mean of the asymmetrical uncertainties is reported in the table. The a_1 coefficient is significantly
 512 lower than past estimates but remain consistent at a 2σ confidence level. The difference may be
 513 due to the lower stellar inclination $i = 45 \pm 4$, that is also only consistent with earlier determination
 514 at 2σ . The a_3 coefficient is marginally greater but with smaller uncertainty than Bazot et al. (2019)
 515 (they reported $a_3 = 11.15 \pm 10.95\text{nHz}$).

516 More importantly, a_2 is positive at 1σ , which is consistent with the assertion of star prolateness
 517 from Bazot et al. (2019) and is inconsistent with the centrifugal distortion term, $a_2^{(CF)}$. Finally, a_4 ,
 518 includes zero within 1σ .

519 With respect to Figures 4-5, $a_1/\Gamma_{\nu_{\text{max}}} = 0.45 \pm 0.04$ and $i = 45 \pm 4^\circ$ place 16 Cyg A in a
 520 parameter space where the expected magnitude of the bias for a_1, a_2 and a_4 is of the order of 0.5σ ,
 521 0.5σ and 0.8σ respectively. This remains accurate even when accounting for the slightly higher
 522 estimates of inclination from previous publications. Translated into absolute units, this corresponds
 523 to approximately $b(a_1) \simeq +10\text{nHz}$ (overestimation), $b(a_2) \simeq -10\text{nHz}$ (underestimation), $b(a_4) \simeq$
 524 -10nHz (underestimation). These fiducial values are used in Section 6.3 to evaluate the effect of
 525 the potential bias on the estimates of the activity zone.

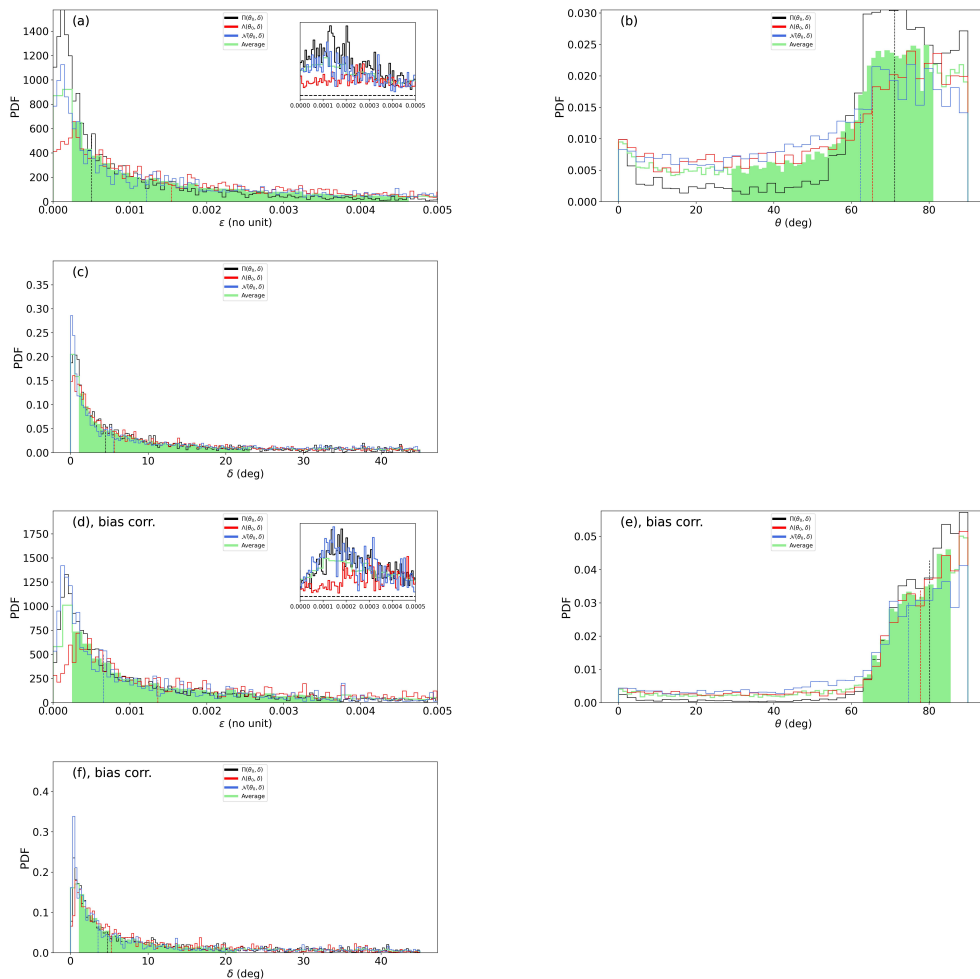


Fig. 11. Inferred pdf for 16 Cyg A for raw measures (a,b,c) or with bias correction (d,e,f). The green curve is for the average pdf with $F = \Pi$, Λ and \mathcal{N} . The shaded area is its 1σ confidence interval. The inset of (a) and (d) is a zoom into the near-zero ϵ values with smaller binning.

6.2. Seismic constraints for 16 Cyg B

526

Similary to 16 Cyg A, 16 Cyg B has around 60 observed modes. However, the reported precision for the past determination of the seismic parameters is less accurate than for 16 Cyg A, despite a similar HNR. Davies et al. (2015) and Bazot et al. (2019) both note a large degeneracy between the stellar inclination and the average rotation rate, with even a clear bi-modality in the distributions obtained by Bazot et al. (2019). Their global solution of $i = 36^{+17}_{-7}$ is associated with two separate solutions for a_1 , centered around ≈ 300 nHz and ≈ 550 nHz, that they use to infer the latitudinal differential rotation profile. Meanwhile, as for 16 Cyg A, the star is found to be prolate, indicating a surface activity.

Figure 12 shows the measured a-coeficients. It appears that including the a_4 coefficient remove the degeneracy issue observed by previous publications. The stellar inclination, a_1 and a_2 are precisely determined and have approximately Gaussian probability distributions and these are reported as such in Table 2. The found rotation rate a_1 correspond to the higher solution of rotational splitting of Davies et al. (2015) and Bazot et al. (2019) (see their Figures of probability density functions). Meanwhile, the degeneracy observed in a_1 in earlier studies is moved to a_4 : It exhibits

527

528

529

530

531

532

533

534

535

536

537

538

539

540

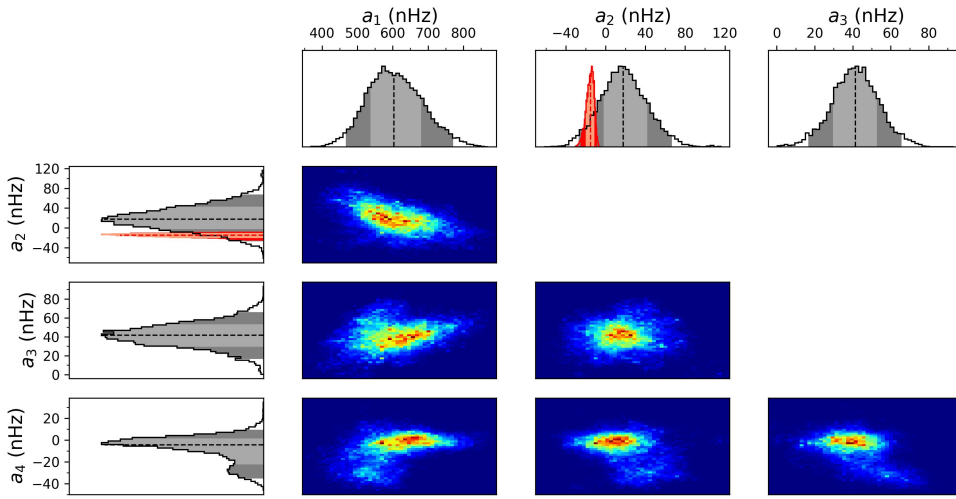


Fig. 12. Probability Density Functions and their correlations, obtained by MCMC of the power spectrum of 16 Cyg B and for coefficients a_1, a_2, a_3, a_4 for 16 Cyg A. The red curve shows the expected a_2^{CF} coefficient for a pure centrifugal distortion of the star. The light and dark gray PDF filling is for the 1σ and 2σ confidence interval, respectively.

541 two solutions. As our method of activity inference assumes Gaussian distributions, the bi-modality
 542 of a_4 requires to separate the two apparent solutions. Using Gaussian mixture modeling (Bishop
 543 1995; Bazot et al. 2019), the mean and standard deviation of both solutions are measured, enabling
 544 their separate analysis. The lowest estimate ($a_4 = -27.9 \pm 6.5\text{nHz}$) weights 30% and the highest
 545 estimate ($a_4 = -1.0 \pm 6.7\text{nHz}$) is more significative as it weights 70%. The inference of the activity
 546 from the two solutions is discussed in Section 6.4. Note that $a_3 = 45_{-14}^{+13}\text{nHz}$ is significantly higher
 547 than the reported values from Bazot et al. (2019) ($a_3 = 13.89 \pm 13.95\text{nHz}$) and may have an impact
 548 on the rotational profile.

549 6.3. Activity inference for 16 Cyg A

550 Figure 11 shows the results from the inference of the activity parameters and a statistical summary
 551 is in Table 3. Triangular and Gaussian descriptions of active latitudes give larger uncertainties than
 552 the simple gate model. However, they all suggest a near-equatorial activity, with a similar detection
 553 significance level of $\simeq 79\%$ (without bias correction) or $\simeq 96\%$ with fiducial correction. As for the
 554 Sun and because the shape of the active region is *a priori* unknown, the average distribution of the
 555 parameters are discussed. The activity intensity has a large uncertainty, but according to the median
 556 of ϵ , may be **between** the maximum and the minimum of solar activity.

557 The posterior probability distribution of δ does not allow us to precisely constrain the extension
 558 of the activity region. As already noted in the case of the Sun, this parameter requires stringent
 559 constraint on both the a_2 and a_4 coefficient in order to inform us about the size of the active region.

6.4. Activity inference for 16 Cyg B

560

Figure 13 and 14 shows the results for the activity for 16 Cyg B in the two possible scenarios of a_4 561
 discussed in Section 6.2 (see Table 3 for the statistical summary). In the case of $a_4 = -27.9 \pm 6.5 \text{ nHz}$ 562
 (Figure 13), the activity is highly significant (greater than 99.3% with or without bias correction, 563
 whatever is the activity zone model) and has stronger intensity than in the case of the Sun. The 564
 active region is then located at $\theta_0 \approx 58^\circ$ ($\theta_0 \approx 60^\circ$, after bias correction), ie. at comparable latitudes 565
 seen during a maximum of activity of the Sun. The bias correction has negligible effect on the 566
 inferred activity latitude. Due to a_4 significantly departing from 0, the extension of active region is 567
 better constrained than in 16 Cyg A or the Sun, but remains weakly informative. 568

The second more likely solution (probability of 70%) corresponds to $a_4 = -1.0 \pm 6.7 \text{ nHz}$ 569
 (Figure 14). It is associated to an activity at co-latitudes above $\approx 40^\circ$ and of lower activity. Its 570
 statistical significance is low, and the activity intensity may be of the same order or lower than 571
 16 Cyg A. In fact, it looks similar to the solar case when approaching its minimum of activity. 572
 Accounting for the fiducial bias, the solution is more concentrated to the equatorial region and 573
 differs significantly from the lower probability a_4 solution. Here, the uncertainty on a_2 and a_4 is 574
 again too large to provide a stringent constraint on the extension of the activity zone δ . 575

7. Discussion and Conclusion

576

The stellar activity is a complex phenomenon **emerging** from the interplay between the stellar 577
 plasma, rotation and magnetism. The activity distorts the shape of mode cavity, perturbing the 578
 pulsation frequencies. This perturbation is here observationally evaluated using a a-coefficient de- 579
 composition. This allows us to separate observables (the a-coefficients) from their physical inter- 580
 pretation (the activity modeling). The separation enables us to demonstrate that the measurements 581
 of the average low a-coefficient, a_2 and a_4 , under some observational conditions, are sufficient to 582
 reveal the presence of a statistically significant activity of similar intensity to the Sun and to deter- 583
 mine its latitude. The required observational conditions are analysed using a methodology similar 584
 to Kamiaka et al. (2018), that is, by constructing a grid of artificial power spectra, that allows us to 585
 determine the bias for a_1 , a_2 and a_4 . It is found that if the height-noise-ratio exceeds 10, the mode 586
 blending factor $f = a_1/\Gamma_{\nu_{max}}$ is greater than 0.4, the inclination is above 30° and that the observation 587
 is longer than 2 years, the inaccuracy remains mild and generally smaller than the 1σ uncertainty. 588
 The uncertainty and/or the inaccuracy may however become too large to reliably detect any activity 589
 beyond the above-specified conditions. In particular and in agreement with Kamiaka et al. (2018), 590
 the stellar inclination is a decisive variable to ensure the accuracy of the measurement. Below 30° , 591
 a_1 is often wrong by a factor 2. This is likely due to the fit mistakenly identifying $l = 2, m = \pm 1$ as 592
 $l = 2, m = \pm 2$ and vice-versa. Other a-coefficients are then severely inaccurate. Therefore, such a 593
 bias analysis suggests that rotation studies of stellar ensembles require a careful star selection. 594

A method that uses the average a_2 and a_4 coefficients is proposed to perform a subsequent 595
 analysis of the activity, considering a geometrical model of the activity effect on the pulsations 596

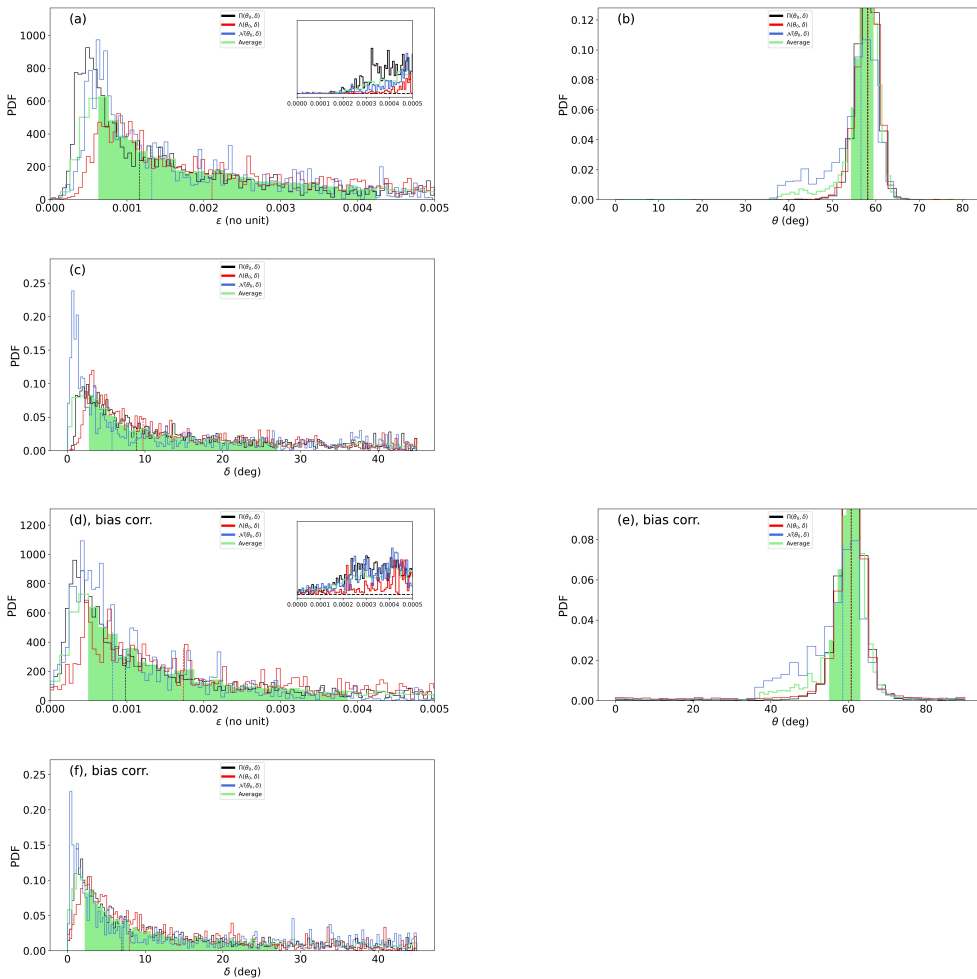


Fig. 13. Inferred pdf of ϵ , θ_0 and δ for raw results of 16 Cyg B with the lower solution $a_4 = -29.2 \pm 5.6\text{mHz}$, without bias correction (a, b, c) or with it (d, e, f). The green curve is for the average pdf with $F = \Pi$, Λ and N . The shaded area is its 1σ confidence interval. The inset of (a,d) is a zoom into the near-zero ϵ values with smaller binning.

597 frequencies and accounting for the stellar asphericity due to the centrifugal effects. This two-step
 598 approach is tested on the case of the Sun and shows that it is effectively able to detect the change
 599 of activity between the solar maximum of activity around 1999-2002 and the minimum of activity
 600 around 2006-2009. Although the use of averaged a-coefficients makes it difficult to evaluate the
 601 extension of the activity zone, the model successfully retrieves the mean latitude of activity during
 602 the maximum of the solar cycle.

603 The method is then applied to the brightest stars observed during the initial observational phase
 604 of the Kepler space instrument, 16 Cyg A and B. These stars were selected as a test-bed due to
 605 the fact that they are well studied and present the highest mode signal-to-noise ratio of all the
 606 currently known main-sequence stars. Davies et al. (2015) suggested that these stars have mild to
 607 no activity. However, Bazot et al. (2019), using a parametric model for describing the asphericity
 608 $(R_{\text{eq}} - R_{\text{pol}})/R_{\text{eq}}$ found an asphericity significant at 1σ . Our current analysis, performed using the
 609 same data set, confirms this asphericity and found a mild (relatively to the Sun) to moderate activity
 610 for both stars. It is found that 16 Cyg A has a near-equatorial band of activity during the period of

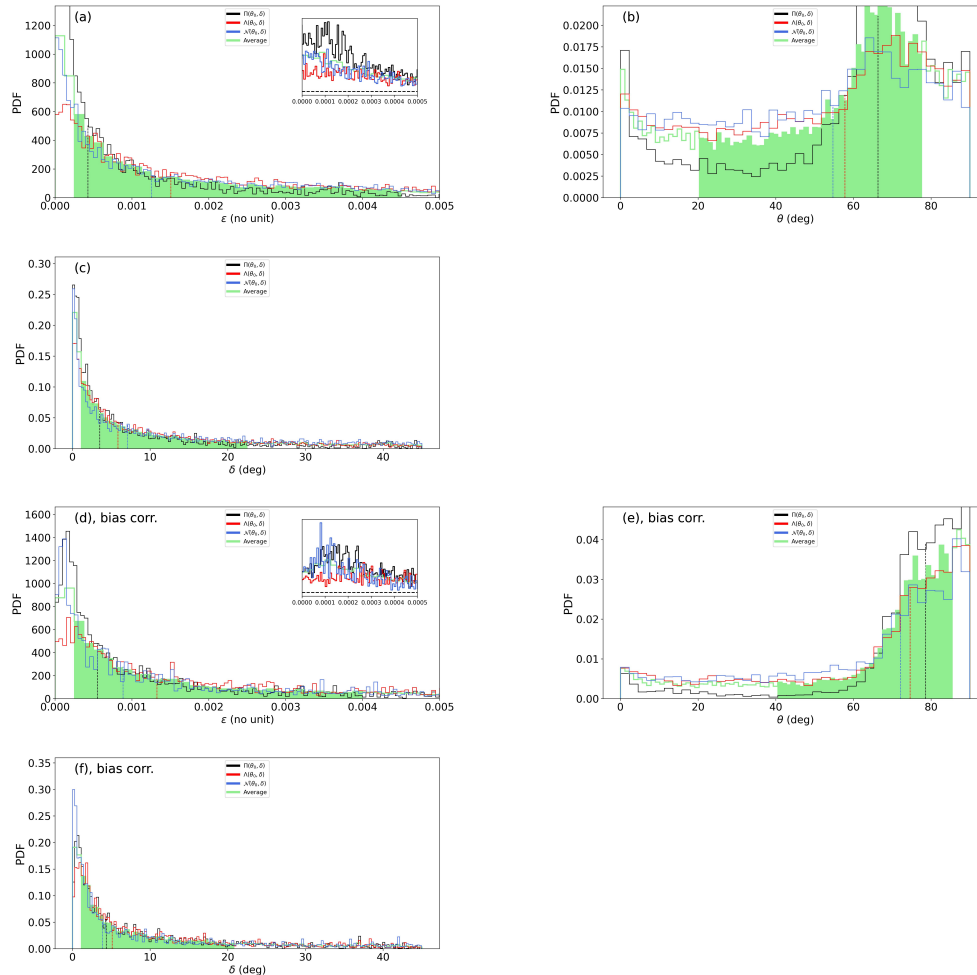


Fig. 14. Same as Figure 13 but for the higher solution $a_4 = -0.9 \pm 6.8\text{nHz}$.

observation (13 September 2010 to 8 March 2013), with a significance of the detection greater than 611
79.8%. 612

The case of 16 Cyg B is more ambiguous. A bi-modality on the average splitting $\langle \delta\nu_{nlm}/m \rangle \simeq a_1$ 613
and on the stellar inclination is already reported in Davies et al. (2015) and Bazot et al. (2019). 614
Our refined model suggests that this bi-modality is in fact related to the $l = 2$ modes. Indeed, as 615
we account for a_1 , a_2 , a_3 and a_4 , we note that the bi-modality previously seen on a_1 in earlier 616
studies is displaced to a_4 . The solutions of a_4 are separated using a Gaussian process algorithm, 617
which found that the weight (or importance) of the highest solution, close to 0 nHz is of 70%. 618
The lower solution, close to -28nHz has a weight of 30%. The associated probability distribution 619
for stellar inclination $i = 35 \pm 3$ is unique (instead of being bi-modal in past studies). The two 620
solutions of a_4 are analysed independently. The lower solution (with lower weight) is associated to 621
an overall activity that is stronger than the Sun, localized at latitudes of approximately 32° (with 622
an uncertainty of $\simeq 3^\circ$). The higher solution is linked to a lower activity and is weakly significant 623
(probability greater than 67.1%). Although the uncertainty is large, the study suggests an activity 624
closer to the equatorial region. In the Sun and as evident in its butterfly diagram, the quiet phase 625
is associated to a magnetic activity closer to the equator, while the transition to the active Sun is 626

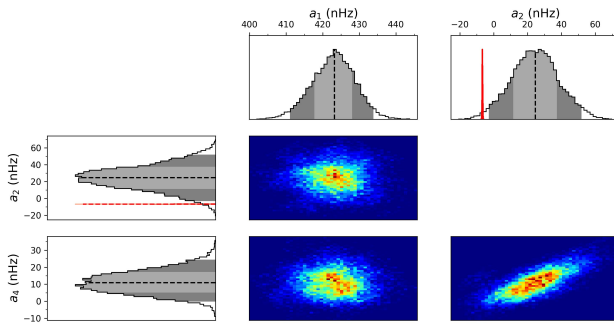


Fig. 15. Probability Density Functions and their correlations, obtained by MCMC for coefficients a_1 , a_2 , a_3 , a_4 for the Sun in-between two activity cycles (2006-2011). The red curve is the expected a_2^{CF} coefficient for a pure centrifugal distortion. The light and dark gray PDF filling is for the 1σ and 2σ confidence interval, respectively.

627 abrupt and characterised by the appearance of magnetic spots at latitudes of 30-40°. In that context
 628 and although it is not possible to rule out the possibility of a statistical fluke, an interpretation of the
 629 bi-modality is that the star was transitioning from a period of low activity to a more active period
 630 during the observation time of the Kepler instrument. To evaluate that hypothesis, we selected solar-
 631 data between Jan 2006 and Jan 2011, including the end of a cycle and the start of a new one. The
 632 measured a-coefficients for that analysis are shown in Figure 15. There is no visible bi-modality
 633 on either a_2 or a_4 . Because 16 Cyg B is evidently different than the Sun, this does not refute the
 634 hypothesis, but weakens it. A more firm verification would require a follow-up observation of the
 635 star, ie with PLATO (Rauer et al. 2014). Or extensive simulations in order to attempt to reproduce
 636 the bi-modality.

637 This work demonstrates that it is possible to determine the latitude and intensity of the activity
 638 for Sun-like stars, when this activity is similar to, or exceed the one of the Sun. The limited observed
 639 bias suggests that the analysis of the stellar activity could also be extended to a larger set of stars.
 640 The Kepler LEGACY stars (Lund et al. 2017) are ideal candidates as these generally satisfy the
 641 criteria of reliability that are discussed in this conclusion and **detailed** in Section 4.

642 Although the a-coefficient analysis has the benefit to allow to simplify the bias studies and to
 643 make the analysis faster, a further axis of improvement would consist in using a single analysis step,
 644 ie, fitting directly the power spectrum with the model of activity. Contrary to the two-step analysis,
 645 such an approach does not require assumptions on the properties of probability distribution of the
 646 a-coefficients as it is currently the case. It would also make use of the full set of a-coefficients
 647 (not only their average), which may lead to smaller uncertainties. However, the two approaches
 648 would certainly be needed in tandem, as the stability of the solution (and its accuracy) is harder to
 649 ascertain when performing a single step fitting approach.

650 O.B. and L.G. acknowledge partial support from NYUAD Institute Grant G1502 "Center for
 651 Space Science". L.G. is supported in part by the European Research Council (ERC) Synergy Grant
 652 WHOLE SUN 810218 and the Max Planck Society grant "Preparations for PLATO Science". We
 653 thank Saskia Hekker for comments and advice. All data presented in this paper were obtained from

the Mikulski Archive for Space Telescopes (MAST) at the Space Telescope Science Institute. The 654
specific observations analyzed can be accessed via [10.17909/T9059R]<https://doi.org/10.17909/T9059R>.

SOHO spacecraft, Kepler spacecraft 656
Analysis tool suite for this paper https://github.com/OthmanB/Benomar2022/tree/version_2 658

659 **Appendix A: Polynomials, a-coefficients and splittings**

660 *A.1. The first six used polynomials*

661 The $\mathcal{P}_j^{(l)}(m)$ coefficients, which are introduced by Schou et al. (1994), can be obtained by normal-
662 izing the $H_j^m(l)$ coefficients by Ritzwoller & Lavelle (1991) so that $\mathcal{P}_j^{(l)}(m = l) = l$.

$$\begin{aligned} \mathcal{P}_j^{(l)}(m) &= \frac{l(2l-j)!}{(2l)!} H_j^m(l) \\ &= (-1)^{-l+m} \frac{l \sqrt{(2l-j)!(2l+j+1)!}}{(2l)!} \begin{pmatrix} j & l & l \\ 0 & m & -m \end{pmatrix} \end{aligned} \quad (\text{A.1})$$

663 in which the last factor means the Wigner $3j$ symbol.

664 They can also be obtained by recurrence using equation (2) and (3), together with the normali-
665 sation condition, $\mathcal{P}_j^l(m) = l$ and starting with $\mathcal{P}_0^l(m) = l$.

666 The first six polynomials are as follows:

$$\mathcal{P}_1^{(l)}(m) = m \quad (\text{A.2})$$

667

$$\mathcal{P}_2^{(l)}(m) = \frac{3m^2 - l(l+1)}{2l-1} \quad (\text{A.3})$$

668

$$\mathcal{P}_3^{(l)}(m) = \frac{5m^3 - (3l(l+1)-1)m}{(l-1)(2l-1)} \quad (\text{A.4})$$

669

$$\mathcal{P}_4^{(l)}(m) = \frac{(35m^4 - 5(6l(l+1)-5)m^2) + 3l(l+1)(l(l+1)-2)}{2(l-1)(2l-1)(2l-3)} \quad (\text{A.5})$$

670

$$\mathcal{P}_5^{(l)}(m) = \frac{252m^5 - 140(2l-3)m^3 + (20l(3l-10)+48)m}{8(4l^4 - 20l^3 + 35l^2 - 25l + 6)} \quad (\text{A.6})$$

671

$$\begin{aligned} \mathcal{P}_6^{(l)}(m) &= \frac{924m^6 - 420m^4(3L-7) + 84m^2(5L^2 - 25L + 14)}{N} \\ &\quad - \frac{20L(L^2 - 8L + 12)}{N} \end{aligned} \quad (\text{A.7})$$

672 where $L = l(l+1)$ and $N = 64l^5 - 480l^4 + 1360l^3 - 1800l^2 + 1096l - 240$.

A.2. Relationship between a-coefficients and splittings

673

The relationships between a-coefficients and symmetric/anti-symmetric splittings can be derived using
equations (4) and (5). These are used to convert model frequencies ν_{nlm} into a-coefficients.

674

A.2.1. Explicit form for low a-coefficients and l=1

676

$$a_1(n, l = 1) = S_{n11} = \frac{\nu_{n,1,1} - \nu_{n,1,-1}}{2} \quad (\text{A.8})$$

677

$$a_2(n, l = 1) = T_{n11}/3 = \frac{(\nu_{n,l,-1} + \nu_{n,l,1})/2 - \nu_{n,l,0}}{3} \quad (\text{A.9})$$

A.2.2. Explicit form for low a-coefficients and l=2

678

$$a_1(n, l = 2) = \frac{S_{n21} + 4S_{n22}}{5} \quad (\text{A.10})$$

679

$$a_2(n, l = 2) = \frac{2T_{n22} - T_{n21}}{7} \quad (\text{A.11})$$

680

$$a_3(n, l = 2) = \frac{S_{n22} - S_{n21}}{5} \quad (\text{A.12})$$

681

$$a_4(n, l = 2) = \frac{T_{n22} - 4T_{n21}}{70} \quad (\text{A.13})$$

A.2.3. Explicit form for low a-coefficients and l=3

682

$$a_1(n, l = 3) = \frac{S_{n31} + 4S_{n32} + 9S_{n33}}{14} \quad (\text{A.14})$$

683

$$a_2(n, l = 3) = \frac{-15T_{n31} + 25T_{n33}}{126} \quad (\text{A.15})$$

684

$$a_3(n, l = 3) = \frac{-S_{n31} - 2S_{n32} + 3S_{n33}}{9} \quad (\text{A.16})$$

685

$$a_4(n, l = 3) = \frac{T_{n31} - 7T_{n32} + 3T_{n33}}{77} \quad (\text{A.17})$$

$$a_5(n, l = 3) = \frac{5S_{n31} - 8S_{n32} + 3S_{n33}}{126} \quad (\text{A.18})$$

$$a_6(n, l = 3) = \frac{15T_{n31} - 6T_{n32} + T_{n33}}{1386} \quad (\text{A.19})$$

688 **Appendix B: Spectrum analysis**689 *B.1. Acoustic-spectrum modelling*

690 The analysis of the asteroseismic data is very often performed by fitting the power spectrum (eg.
 691 Appourchaux et al. 1998, 2008). This requires to devise a likelihood function and a model for the
 692 observed spectrum. As our fitting involves a Bayesian approach, the priors are also required.

693 *B.1.1. Likelihood*

694 The likelihood function is determined by the noise statistics of the power spectrum, which is a χ^2 -
 695 squared with two degree of freedom. It is also based on the assumption that the frequency bins are
 696 independent and uncorrelated. This implies that the observation duration is assumed to be much
 697 greater than the typical lifetime of the pulsation modes and that the duty cycle is sufficient to allow
 698 us to neglect any leakage induced by the window function. The observation timeframe for the
 699 LEGACY sample is of the order of years, which is significantly longer than the mode lifetime.
 700 Furthermore, the duty cycle is above 95%, which was shown to be sufficient to neglect leakage
 701 (Stahn 2010). Under these conditions, the likelihood function is (Anderson et al. 1990),

$$L_1(S(\nu_i)|X, M) = \sum_{i=0}^{N-1} \frac{1}{S(\nu_i)} \exp\left(-\frac{S(\nu_i)}{M(\nu_i, X)}\right) \quad (\text{B.1})$$

702 where $S(\nu_i)$ is the power at the central frequency ν_i of the i^{th} bin. Here, N is the total number of
 703 bins and $M(\nu_i, X)$ is the model of the power spectrum with the set of variable X for the model M .

704 From Bayes theorem, the posterior probability density function is defined as,

$$\pi_1(X|S(\nu), M) = \frac{\pi_1(X|M) L_1(S(\nu)|X, M)}{\pi_1(S(\nu)|M)} \quad (\text{B.2})$$

705 where $\pi_1(X|M)$ is the prior knowledge on the parameters X . $\pi_1(S(\nu)|M)$ is a normalization constant,
 706 essential only for comparing the significance of models (eg. Gregory 2005; Benomar et al. 2009).
 707 Variables are assumed to be independent from each others. This implies that the joint prior is the
 708 product of individual priors. The posterior is evaluated using the Tempered Adaptive MCMC code⁹
 709 described in Atchadé (2006) and implemented by Benomar (2008).

⁹<https://github.com/OthmanB/Benomar2022/Programs/TAMCMC-1.81>

B.1.2. Acoustic spectrum model

710

The model used for the power spectrum fitting, involves a sum of asymmetrical Lorentzian, superimposed to a monotonically decreasing function of frequency (pink noise). The asymmetric Lorentzian is commonly used in helioseismology (Duvall et al. 1993; Nigam & Kosovichev 1998; Georgobiani et al. 2000; Toutain et al. 1998) and in asteroseismology for Sun-like stars (Benomar et al. 2018b),

$$M(\nu) = \sum_{n=n_0}^{n_{\max}} H_{nlm} \frac{(1 + B_{nlm} z)^2 + B_{nlm}^2}{1 + z^2} + N(\nu), \quad (\text{B.3})$$

with $z = 2(\nu - \nu_{nlm})/\Gamma_{nlm}$. Each asymmetrical Lorentzian is defined by a height H_{nlm} , width Γ_{nlm} , a central frequency ν_{nlm} and an asymmetry B_{nlm} . As explained by Gizon (2006); Benomar et al. (2018b), the asymmetry coefficient depends on the mode width and frequency. The normalized asymmetry coefficient $\chi_{nlm} = 2 \frac{B_{nlm} \nu_{nlm}}{\Gamma_{nlm}}$ is fitted instead as it is nearly constant over the range of fitted modes.

Several prescriptions exist for describing the noise background $N(\nu)$. Here, it is assumed to be a sum of two generalized Lorentzian, sometimes referred as Harvey-like profiles (Harvey 1985), and of a white noise,

$$N(\nu) = \frac{A_1}{1 + (\tau_1 \nu)^{p_1}} + \frac{A_2}{1 + (\tau_2 \nu)^{p_2}} + N_0. \quad (\text{B.4})$$

Here N_0 is the white noise and A_k is the maximum heights of the k^{th} generalized Lorentzian. The τ_k parameter is timescale that is the inverse of the full width at half maximum of the Lorentzians, and p_k is a power exponent.

The fit is performed globally over all the statistically significant peaks visible in the power spectrum of a star. This can lead to a very large number of fitted parameters (up to a few thousands), which is practically unsuitable. A model simplification is therefore preferred, similar to eg. Appourchaux et al. (2008); Benomar et al. (2009); Campante et al. (2011); Handberg & Campante (2011) with main simplifications recalled hereafter,

- The m dependence on heights is controlled by its relationship with the stellar inclination (Gizon & Solanki 2003). This saves several hundreds of parameters.
- The relative height of the different degree l is constant across the fitted range and for a given l , hence $V_l^2 = H_{n,l}/H_{n,l=0} = \text{const}$. Only the $l = 0$ heights $H_{n,l=0}$ are variables. The mode visibility V_l^2 replaces the $H_{n,l>0}$ as a variable.
- Given a degree l , $\Gamma_{n,l,m} = \Gamma_{n,l}$ is imposed. This is justified by the fact that the width depends weakly on the frequency: all splitted components are assumed to have the same width.
- Because $\Gamma_{n,l}$ is nearly independent of the degree, it is possible to fit $\Gamma(\nu) = \Gamma_{n,l=0}$ and interpolate it to the frequencies of the modes with degree $l > 0$.

These assumptions reduce the number of variables to a few tens in the case of CoRoT, Kepler or TESS observations. The frequencies of the modes follow equation (14) in Section 2.3.

743 **B.2. Priors**

744 Priors are fundamental of a Bayesian method. This section explicits $\pi_1(X|M, I)$, the prior used
 745 during the power spectrum fitting. Parameters of the vector X are assumed independent to each
 746 others, such that the product rule is used to define $\pi_1(X|M, I)$.

Main mode parameters						
Height ($ppm^2/\mu\text{Hz}$)	Width (μHz)	Frequency (μHz)	Asymmetry ($ \chi $)	$V_{l=1}^2$	$V_{l=2}^2$	inclination
$\mathcal{J}(1,1000)$	$\mathcal{J}(0.1, 45)$	$\mathcal{U}(\nu_{\min}, \nu_{\max})$	$\mathcal{J}(5, 100)$	$\mathcal{G}(1.5, 0.15)$	$\mathcal{G}(0.53, 0.053)$	$\mathcal{U}(0,90)$

Table B.1. Mode priors used for the fit of the power spectrum. Prior parameters on frequencies are visually determined, see Section B.2.

747 Heights, widths, frequencies, asymmetry and inclination use non-informative priors. These are
 748 either Jeffreys priors for scale parameters, noted $\mathcal{J}(x_{\min}, x_{\max})$ or uniform prior, noted $\mathcal{U}(x_{\min}, x_{\max})$.
 749 Priors on frequencies are uniform and require a visual inspection of the power spectrum in order to
 750 assign the lower and upper bound of the prior for each mode that follow the expected pattern for
 751 main sequence Sun-like stars (equally spaced p modes) and that show an excess of power relative
 752 to the background that exceeds 80%. The excess of power is determined using a smooth spectrum
 753 for which the noise statistics is derived by Appourchaux (2003). Mode visibilities are defined by
 754 Gaussian priors (noted $\mathcal{G}(x_0, \sigma)$), with mean x_0 set as the solar value (see Ballot et al. 2011) and
 755 the standard deviation σ is 10% of the mean. Table B.1 lists the type and the prior characteristic
 756 values that are used for the parameters of the modes.

757 The prior on a_1 is uniform between 0 and 1500 nHz. For 16 Cyg A and B, an uniform fixed prior
 758 is set on $|a_3|$ over the range [0, 100] nHz. However at each iteration of the optimisation process, $|a_3|$
 759 is not allowed to exceed 20% of a_1 . Preventing extremely large relative value of a_3/a_1 , improves
 760 the fit stability and ensure a faster convergence of the algorithm. For the Sun analysis and because
 761 it is not possible to measure a_3 for $i \approx 90^\circ$ (due to the lack of amplitude of $l = 2, m = \pm 1$ at that
 762 inclination), a_3 is fixed to 0.

763 The priors on a_2 and a_4 are also uniform. The range is defined by using the maximum range
 764 of Figure 3 (showing $a_2^{(AR)}$ and $a_4^{(AR)}$), increasing it by 50% and adding the expected centrifugal
 765 term $a_2^{(CF)}$, assuming $a_1 = 400\text{nHz}$ for the Sun and $a_1 = 600\text{nHz}$ for 16 Cyg A/B. The $\Delta\nu$ reported
 766 in Table 2 is also used. For the same reason as to a_3 , a_2/a_1 cannot exceed 50% and a_4/a_1 cannot
 767 exceed 20% at each iteration step of the optimisation process.

768 The noise priors are obtained from a global MAP approach similar to Benomar et al. (2012).
 769 This provides the best fit values and 1σ uncertainties that are used as priors. The noise background
 770 of the individual model analysis is described by equation (B.4). During the global MAP fit, the
 771 model is made of that same background model, plus a Gaussian envelope to account for the power
 772 excess due to the modes (eg Mathur et al. 2010; Huber et al. 2011).

Appendix C: Inference of the active latitudes

773

The determination of the activity is performed as a second step using as observables the marginalised posterior distribution of the average a-coefficients. This section describes the method and assumptions to determine the posterior distribution and to compute the significance of the detection. 774
775
776

C.1. Posterior distribution and likelihood

777

Similarly as to the power spectrum fitting described in Section B, the determination of the most likely latitudes for the activity and its significance necessitate the computation of a posterior distribution, 778
779
780

$$\pi_2(\mathbf{X}|\mathbf{O}, M) = \frac{\pi_2(\mathbf{X}|M) L_2(\mathbf{O}|\mathbf{X}, M)}{\pi_2(\mathbf{O}|M)}, \quad (\text{C.1})$$

with $\pi_2(\mathbf{X}|\mathbf{O}, M)$, $\pi_2(\mathbf{X}|M)$, $L_2(\mathbf{O}|\mathbf{X}, M)$ are the posterior distribution, the prior, the likelihood, respectively. The denominator $\pi_2(\mathbf{O}|M)$ is the normalisation constant used for model comparison (marginal likelihood). The posterior distributions of the a-coefficients $a_{2,o}$ and $a_{4,o}$ obtained by power spectrum fitting are the observables contained in \mathbf{O} . The class of the model is identified by the variable M . 781
782
783
784
785

For simplicity, the observables are assumed to be distributed according to un-correlated gaussians functions, such that $\mathbf{O} = \{a_{2,o}, a_{4,o}, \sigma_{2,o}, \sigma_{4,o}\}$, where $a_{2,o}$ and $a_{4,o}$ are the mean for the distributions of a_2 and a_4 while $\sigma_{2,o}$, $\sigma_{4,o}$ are the standard deviations. This leads to a log-Likelihood in the form of a χ^2 -squared, 786
787
788
789

$$\ln L_2(\mathbf{X}|\mathbf{O}, M) = -\frac{(a_{2,o} - a_{2,m}(\mathbf{X}))^2}{2\sigma_{2,o}^2} - \frac{(a_{4,o} - a_{4,m}(\mathbf{X}))^2}{2\sigma_{4,o}^2}. \quad (\text{C.2})$$

In Dziembowski et al. (2000), a-coefficients are weighted using the inverse of the mode inertia (see their equation 4). This is due to the fact that the inertia account for most of the frequency-variations of the coefficients. It is essentially relevant if the uncertainties are small enough to observe a trend when modes are fitted individually. However, in the case of the Sun and with either GOLF or BiSON data, it is difficult to perceive a frequency-trend (Chaplin et al. 2003). Our own trials on VIRGO/SPM using a linear fit to describe the frequency dependence of a-coefficient did not detect a slope that is significant at more than 1σ . A similar analysis on 16 Cyg A and B and on simulations showed evidence of large uncertainties when attempting to determine frequency-variations for stars with HNR typical of Kepler observations. In fact, only the average the a-coefficient over l and n is shown to be robustly determined (see also our discussion Section 3.3) so that inertia effects are here neglected. 790
791
792
793
794
795
796
797
798
799
800

801 The activity model M_{AR} depends on the variables $\mathbf{X} = \{\epsilon, \theta_0, \delta\}$ and $a_{2,m}(\mathbf{X})$, $a_{4,m}(\mathbf{X})$ denote the
 802 modeled a-coefficients. The log-likelihood is then,

$$\ln L_2(a_{2,o}, a_{4,o}, \sigma_{2,o}, \sigma_{4,o} | a_{2,m}, a_{4,m}, M_{AR}) = -\frac{(a_{2,o} - a_{2,m}(\epsilon, \theta_0, \delta))^2}{2\sigma_{2,o}^2} - \frac{(a_{4,o} - a_{4,m}(\epsilon, \theta_0, \delta))^2}{2\sigma_{4,o}^2}. \quad (\text{C.3})$$

803 In our case, the observables are the average of the fitted modes coefficients, $a_{2,o} = a_2^{(CF)} + a_2^{(AR)}$
 804 and $a_{4,o} = a_4^{(AR)} = 0$. However, to conveniently propagate all errors on the parameters of $a_2^{(CF)}$
 805 ($a_1, \Delta\nu, \Delta\nu_\odot, \rho_\odot, \nu_{nl}$), it is preferable to use $a_{2,o} = a_2^{(AR)}$, obtained by subtracting the $a_2^{(CF)}$ from
 806 the a_2 measured by power spectrum fitting. The distribution of $\Delta\nu$ is computed by linear fitting
 807 of the group-wise ensemble of samples ($n, l = 0$) for each measured frequencies ν_{n0} . The term
 808 $a_2^{(CF)}$ is finally obtained by weighted average of all independent $a_2^{(CF)}(n, l)$ computed at the star's
 809 posterior frequencies ν_{nl} . The subtraction of $a_2^{(CF)}$ is then again performed using the samples of
 810 its posterior, enabling to construct of the posterior probability distribution function of $a_2^{(AR)}$, from
 811 which we deduce its mean $a_{2,o}$ and its standard deviation $\sigma_{2,o}$. To evaluate the relevance of the
 812 activity, two models are considered. First, a model ($M = M_{CF}$) without activity, that accounts only
 813 for the centrifugal effects and second, a model ($M = M_{AR}$) with activity. Their details and the
 814 choice of the priors is described in the following sections for each of them.

815 C.2. Model without activity M_{CF}

816 The model M_{CF} has no unknown variable that require minimisation, see equation (13). For the sake
 817 of the model comparison with the model M_{AR} , it is however important to determine the marginal
 818 likelihood of M_{CF} . From that perspective, it is necessary to calculate the denominator of equation
 819 (C.1), $P(\mathbf{O}|M_{CF})$ which is defined as an integral,

$$P(\mathbf{O}|M_{CF}) = \int \pi(\mathbf{X}|M_{CF}) L_2(\mathbf{O}|a_{2,m}, a_{4,m}, M_{CF}) d\mathbf{X}. \quad (\text{C.4})$$

820 An absence of activity correspond to the limit case where the a-coefficients of the activity are
 821 exactly 0. This corresponds to setting dirac priors on $a_{2,m} = \delta_0$ and $a_{4,m} = \delta_0$ and implies that the
 822 marginal likelihood is the local value of the likelihood at $\mathbf{X} = \{0, 0\}$. The model comparison is
 823 commonly performed in log-space such that,

$$\ln P(a_{2,o}, a_{4,o}, \sigma_{2,o}, \sigma_{4,o} | M_{CF}) = -\frac{a_{2,o}^2}{2\sigma_{2,o}^2} - \frac{a_{4,o}^2}{2\sigma_{4,o}^2}. \quad (\text{C.5})$$

C.3. Model with activity M_{AR}	824
-----------------------------------	-----

Regarding the model with activity of equation (C.3), priors must then be set on the variables subject to optimisation. The ϵ and δ parameters are indispensable intensive parameters and the adequate non-informative prior is then the (truncated) Jeffreys prior (Jeffreys 1961), uniform in the log-space, 825
826
827
828

$$J(x) = \frac{\ln(1 + x_{max}/x_{min})}{x + x_{min}}, \quad (\text{C.6})$$

where x_{min} , x_{max} are upper and lower bounds such that if $x > x_{max}$ or $x < x_{min}$ then $J(x) = 0$. 829
This guarantees that the probability density is proper (the integral over x is finite). In case of weak 830
information content in the observables, this prior is more weighted toward a null-value. We set 831
 $\epsilon_{min} = 5.10^{-4}$ and $\epsilon_{max} = 10^{-2}$. This embraces the solar value $\epsilon \simeq 5.10^{-4}$ (Gizon 2002). Because 832
at the maximum of solar activity, $\delta \simeq 10^\circ$, we set $\delta_{min} = 10^\circ$. Note also that consistently with the 833
discussion on Figure 2 of Section 3, $\delta_{max} = 45^\circ$ is required. Finally, the location parameter θ_0 has 834
an uniform prior in the range $[0, 90]^\circ$. 835

The marginal likelihood of the model M_{AR} requires us to evaluate the triple integral, 836

$$P(\mathbf{O}|M) = \int \pi(\epsilon) \pi(\theta) \pi(\delta) L_2(\mathbf{O}|a_{2,m}, a_{4,m}, M) d\epsilon d\theta d\delta. \quad (\text{C.7})$$

The MCMC process used here involves the use of parallel Metropolis-Hastings tempered chains. 837
The chains are mixing each other in order to enhance the sampling. As explained in Benomar 838
et al. 2009, see their Section A.3, these parallel chains can be used to approximate the equation 839
(C.7). This technique is here used with 10 parallel chains following a geometrical temperature law 840
 $T_k = 1.7^{k-1}$, with k , the chain index such that $k = 1$ is the target distribution, given by equation 841
(C.1). 842

Appendix D: Bias map for $\widehat{HNR} = 10$ and $\widehat{HNR} = 20$

This section shows the bias on the a_1 , a_2 and a_4 coefficients in the case of $\widehat{HNR} = 10$ or $\widehat{HNR} = 20$. 844
The figure D.1 and D.3 are for the case of an equatorial band of activity and figure D.2 and D.4, for 845
a polar cap. It is noticeable that the inaccuracy of the fit remains smaller than standard deviation in the 846
majority of the parameter space and for $i > 30^\circ$, $a_1/\Gamma_{v_{max}} > 0.4$. Interestingly, the relative-to-error 847
bias on a_1 is more pronounced in the case of an equatorial band of activity and for $\{a_1/\Gamma_{v_{max}} \leq 848$
 $0.4, i = [30, 60]\}$ (Figure D.1d and D.3d) and can exceed 3 times the uncertainty. The accuracy 849
of the inference of activity based on the a-coefficients is expected to weakly depend on the \widehat{HNR} 850
(although potentially with large uncertainty) for most stars, except within this regime (in addition 851
to the gray area), where the centrifugal effect will be overestimated. 852

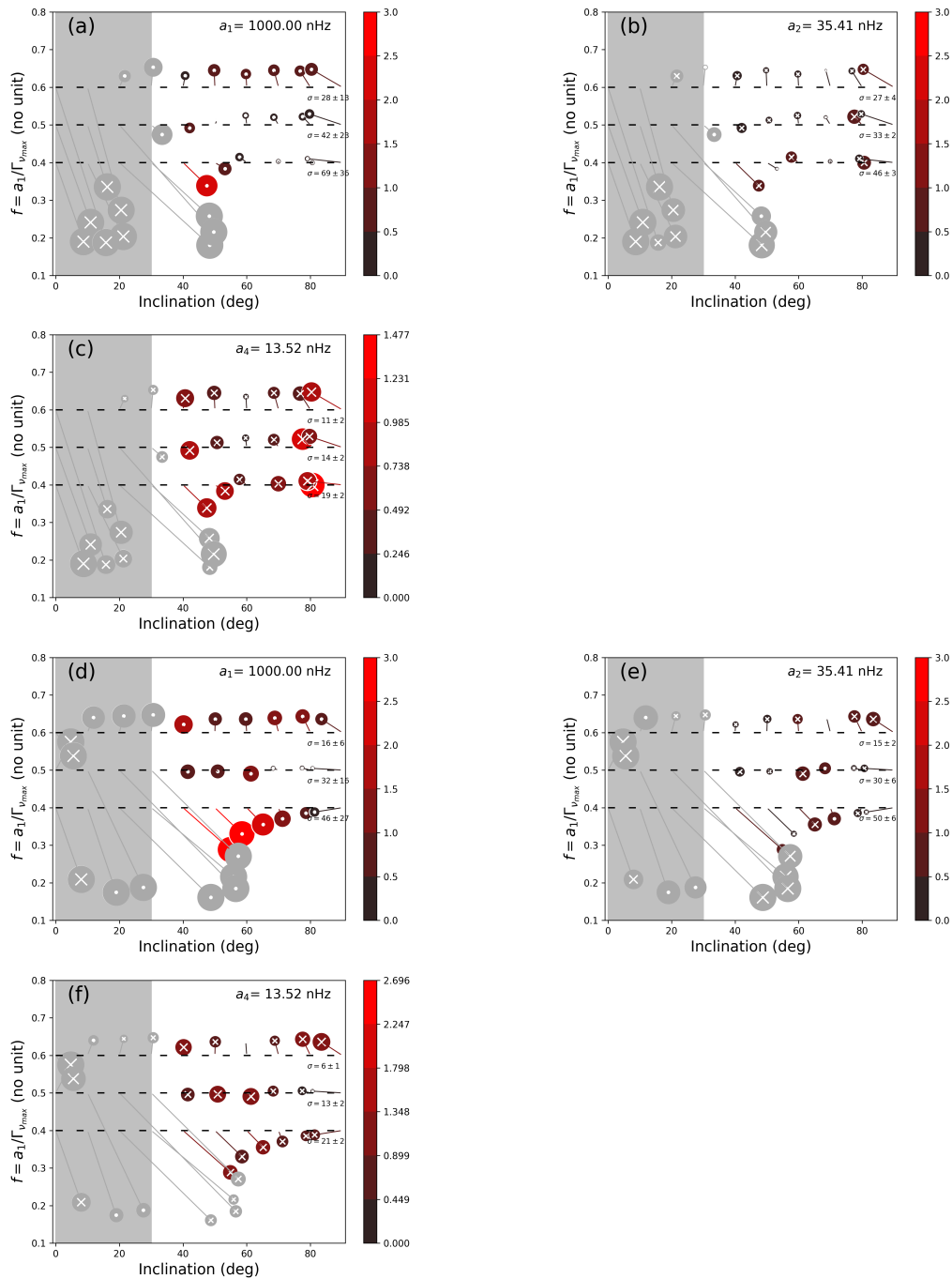


Fig. D.1. Bias analysis for $\widehat{HNR} = 10$ for an equatorial activity band ($\theta_0 = 85, \delta = 10$) of similar intensity to the Sun ($\epsilon_{nl} = 5.10^{-4}$), for $T_{obs} = 2$ years (top) and $T_{obs} = 4$ years (bottom).

853 Appendix E: Figures of the best fits

854 This section presents visuals on the best MCMC fits for the power spectrum of the active Sun
 855 (Figure E.1), quiet Sun (Figure E.2), 16 Cyg A (Figure E.3) and for the two a_4 solutions of 16 Cyg
 856 B (Figures E.4 and E.5). For 16 Cyg B, the solutions are here separated by selecting the median
 857 for the samples only below or above $a_4 = 21$ nHz. In the case of the Sun, the impact of the activity
 858 on the profile of $l = 2$ is very clear, as the shifts of the m-components introduces an asymmetry in

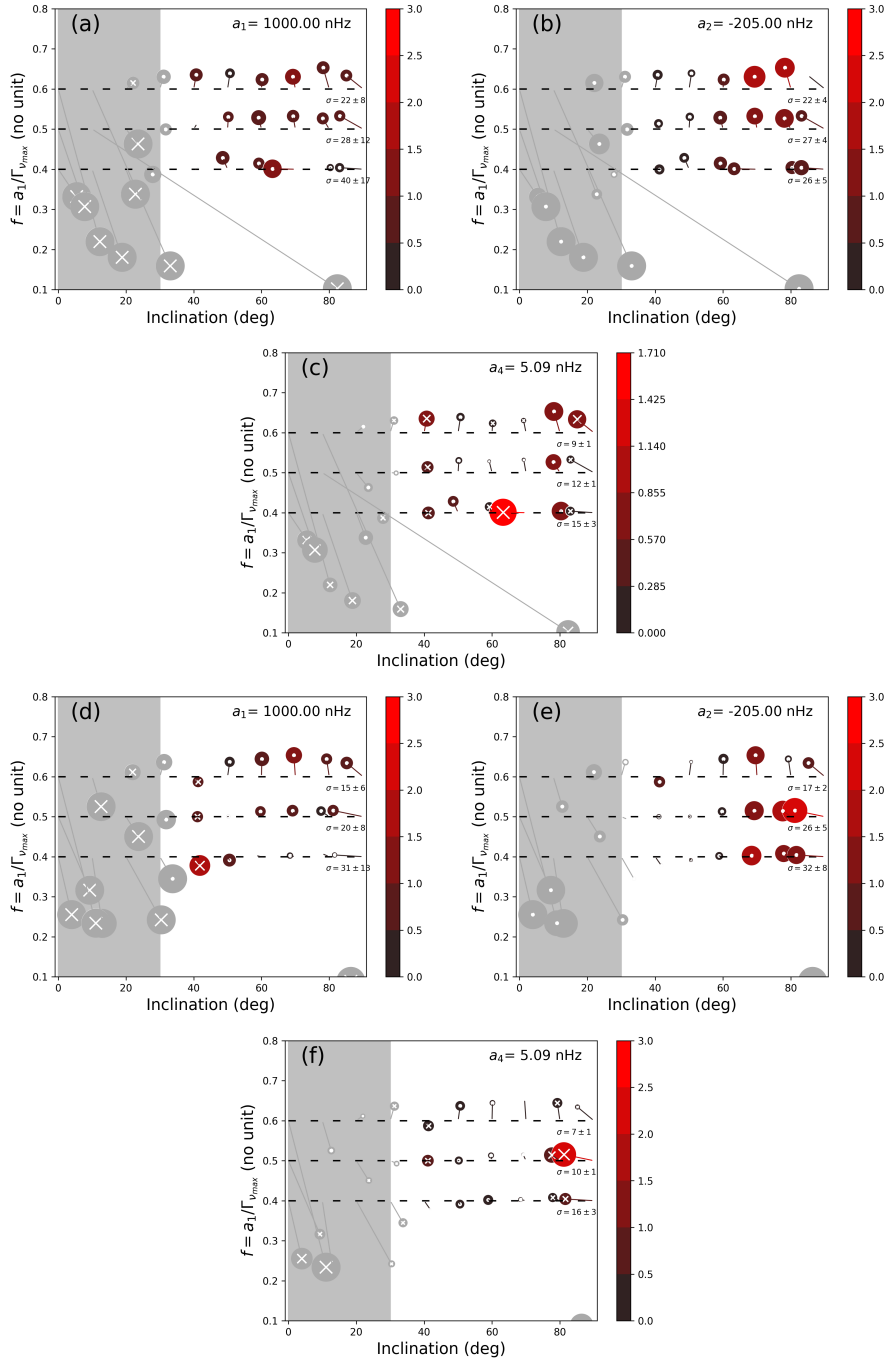


Fig. D.2. Bias analysis for $\widehat{HNR} = 10$ for a large polar activity cap ($\theta_0 = 22.5^\circ, \delta = 45^\circ$) of similar intensity to the Sun ($\epsilon_{nl} = 5.10^{-4}$), for $T_{obs} = 2$ years (top) and $T_{obs} = 4$ years (bottom).

power for the overall $l = 2$ mode profile during the active phase. During the quiet phase such an asymmetry is not visible. 859

Similarly and although it is less pronounced than in the Sun, in the case of 16 Cyg A and B, a weak asymmetry is visible on $l = 2$ modes. For 16 Cyg B, the two solutions of a_4 provide sensibly similar mode profiles as the difference is weakly apparent to the eye only for $l = 2$. The residuals do not show striking differences. This visually supports the fact that goodness of the fit is similar and explain that the two solutions co-exists in statistical terms. 861
862
863
864
865

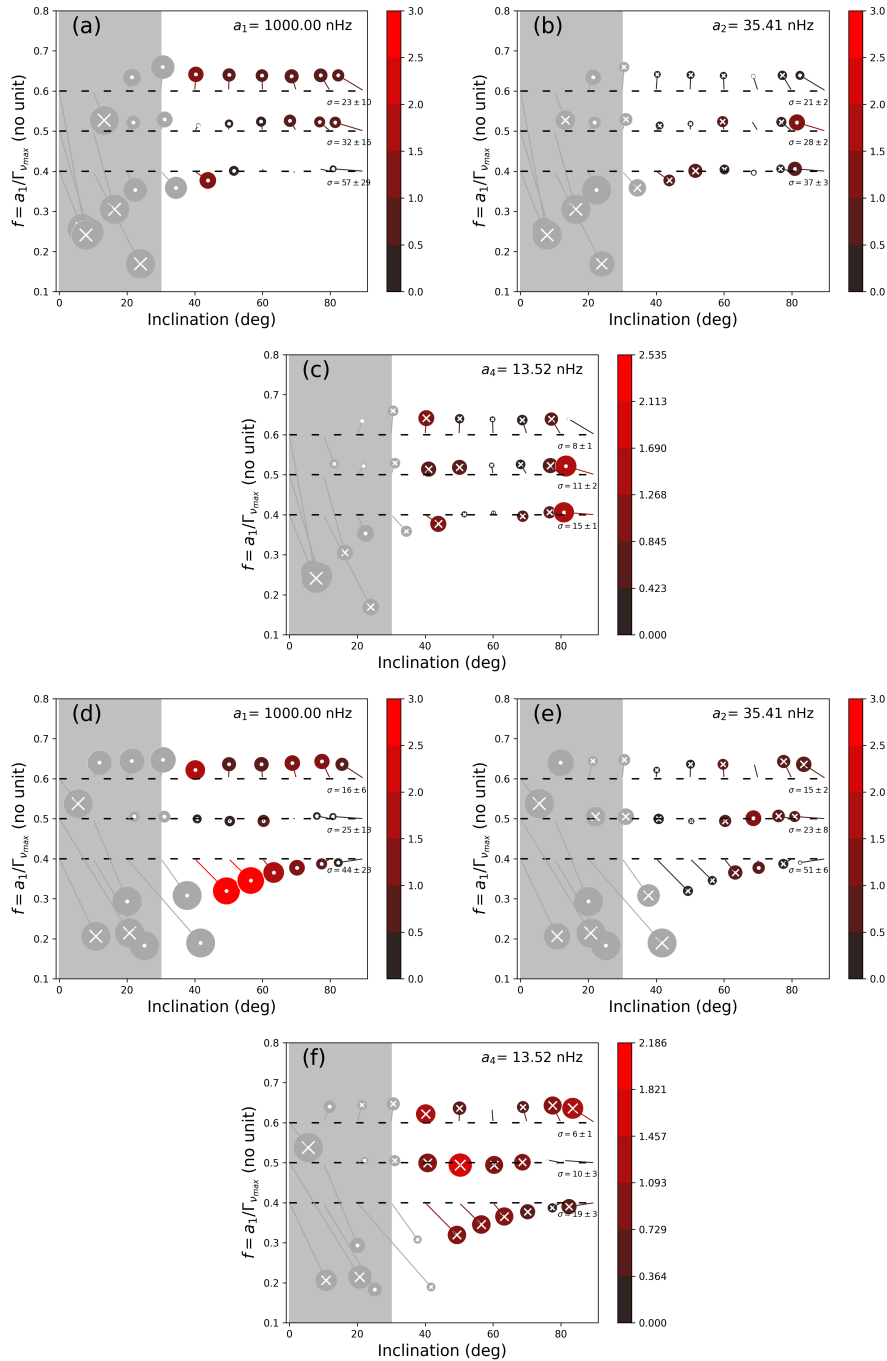


Fig. D.3. Bias analysis for $\widehat{HNR} = 20$ for an equatorial activity band ($\theta_0 = 85, \delta = 10$) of similar intensity to the Sun ($\epsilon_{nl} = 5.10^{-4}$), for $T_{obs} = 2$ years (top) and $T_{obs} = 4$ years (bottom).

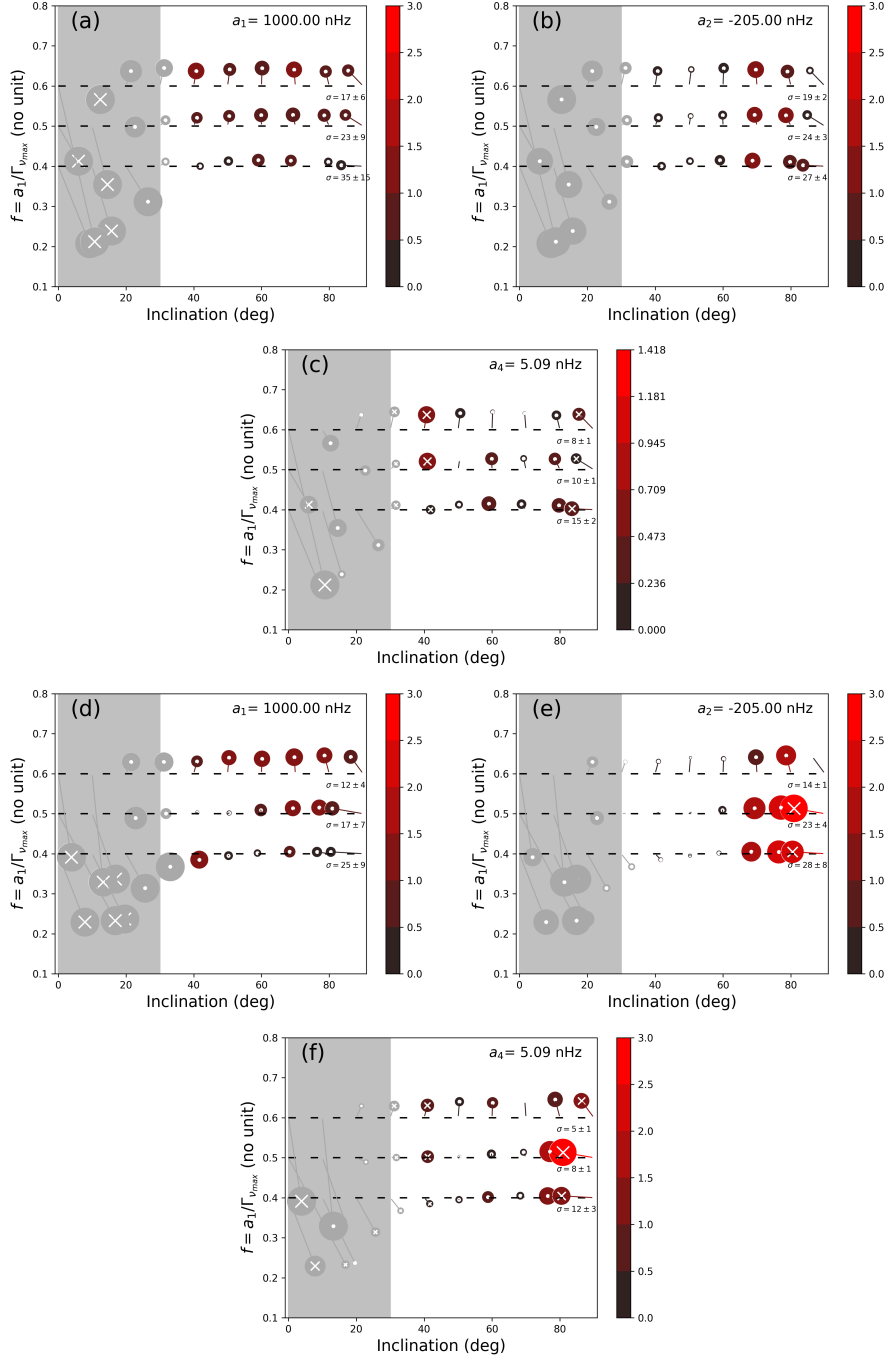


Fig. D.4. Bias analysis for $\widehat{HNR} = 20$ for a large polar activity cap ($\theta_0 = 22.5, \delta = 45$) of similar intensity to the Sun ($\epsilon_{nl} = 5.10^{-4}$), for $T_{obs} = 2$ years (top) and $T_{obs} = 4$ years (bottom).

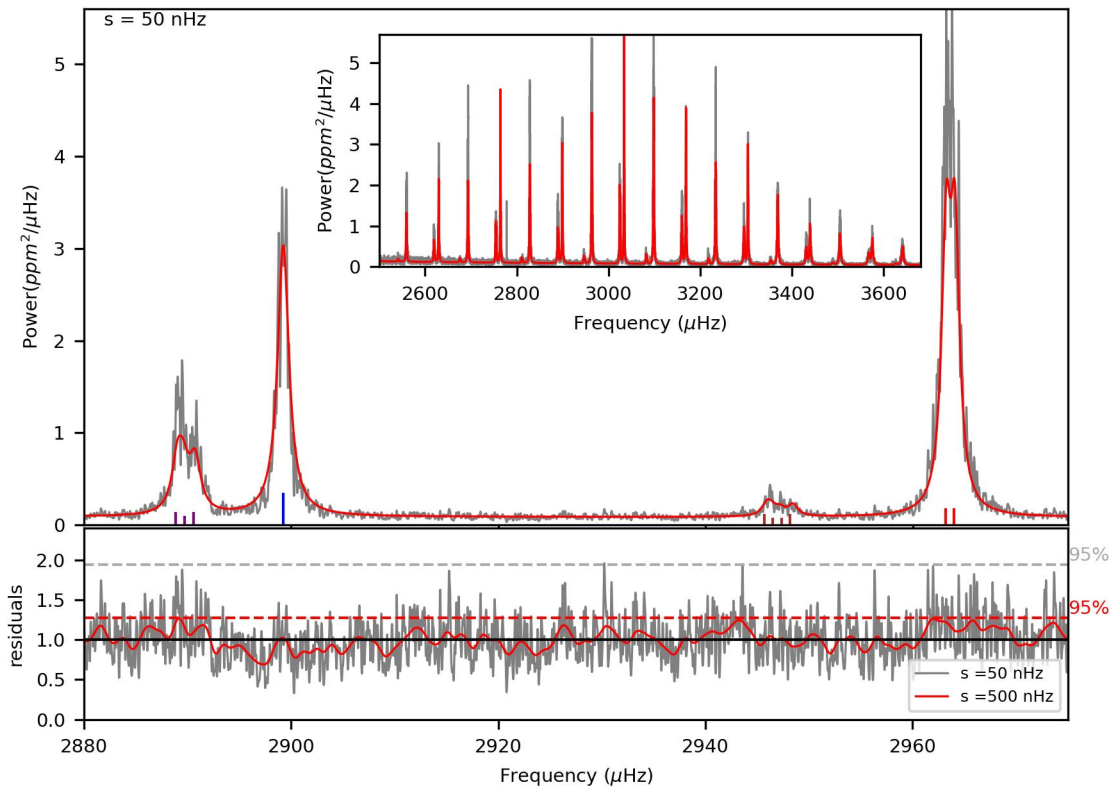


Fig. E.1. Solar power spectrum for observation between 1999 and 2002 after Gaussian smoothing over a kernel width $s=50\text{ nHz}$. Superimposed is the best MCMC fit. Top. Highlight of a $l = 2, 0, 3, 1$ mode group (left to right) and their fit (red). The power asymmetry due to non-symmetric m components is visible in the data. Inset. Overall view of the modes. Bottom. Residual of the fit with two level s of gaussian smoothing.

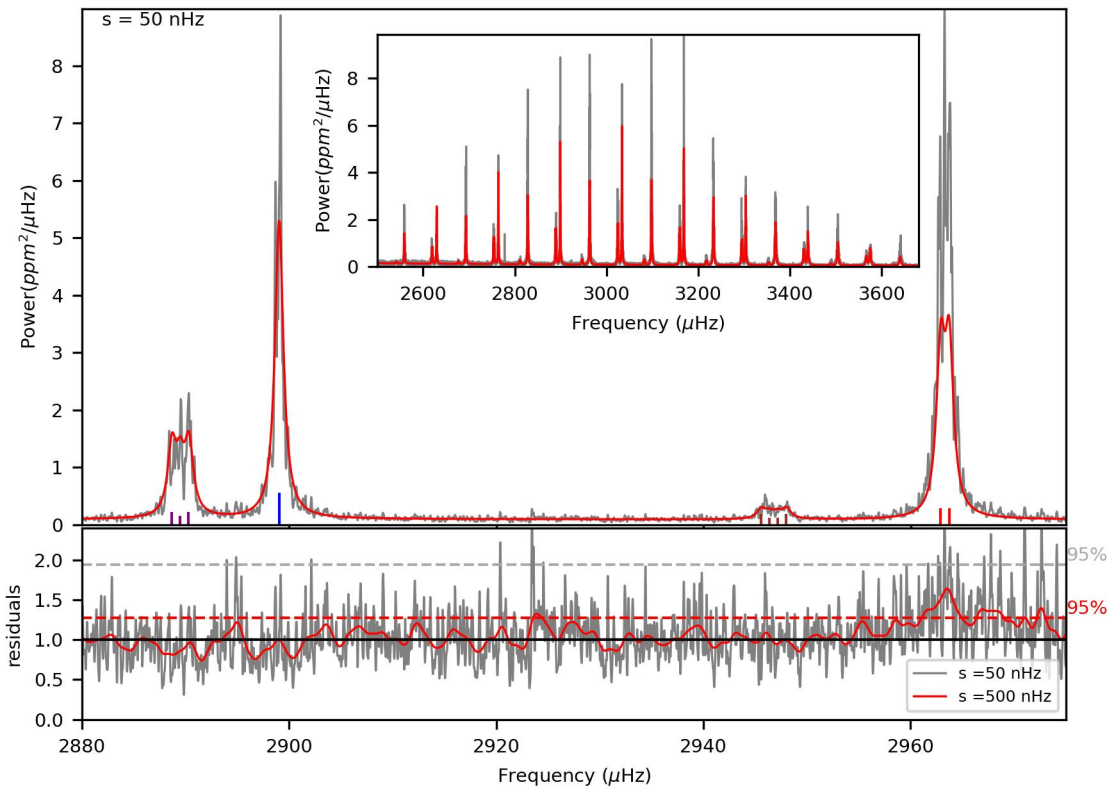


Fig. E.2. Same as Figure E.1 but between 2006 and 2009. Top. Highlight of a $l = 2, 0, 3, 1$ mode group (left to right) and their fit (red). The power asymmetry seen for 1999–2002 is not apparent in the data. Inset. Overall view of the power spectrum. Bottom. Residual of the fit with two level s of gaussian smoothing. The residual on $l = 1$ is a bit high here due to the fix visibility for all modes.

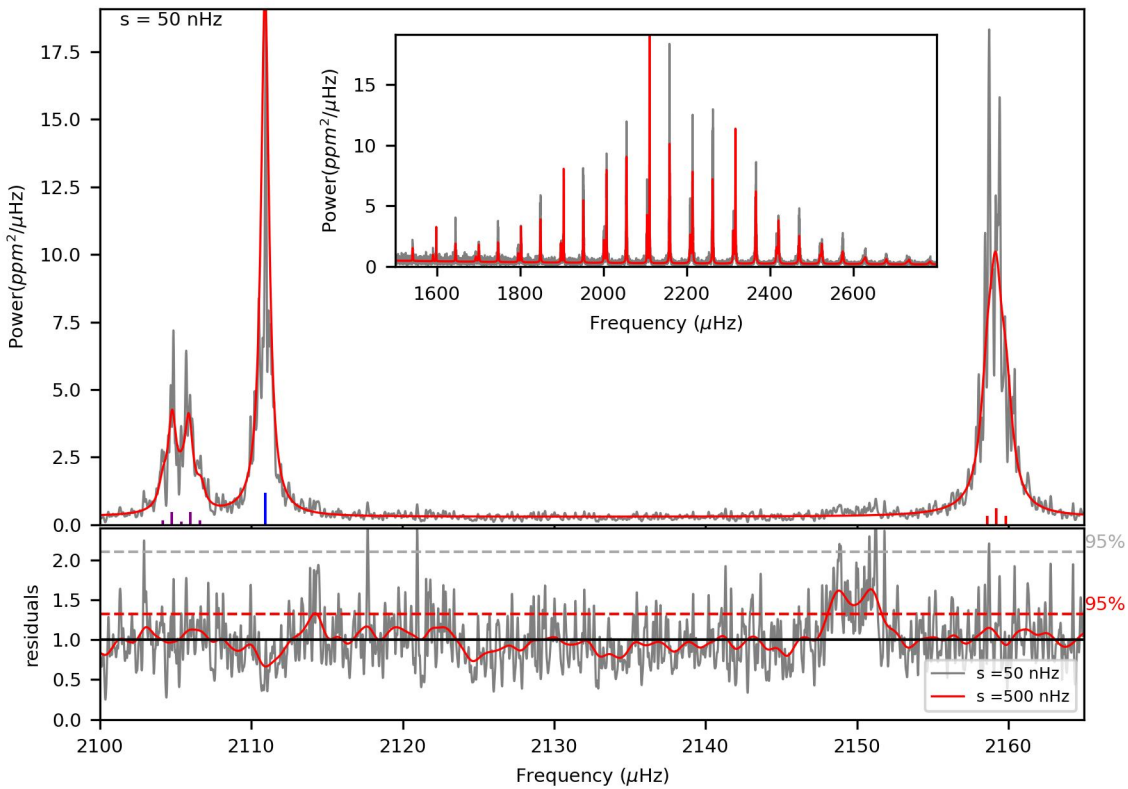


Fig. E.3. Same as Figure E.1 but for 16 Cyg A. Top. Highlight of a $l = 2, 0, 1$ mode group (left to right) and their fit (red). A very mild power asymmetry is seen on the $l = 2$ data. Inset. Overall view of the power spectrum. Bottom. Residual of the fit with two level s of gaussian smoothing. The residual show an excess of power due to the low HNR $\simeq 1.7$ $l = 3$ (not fitted here).

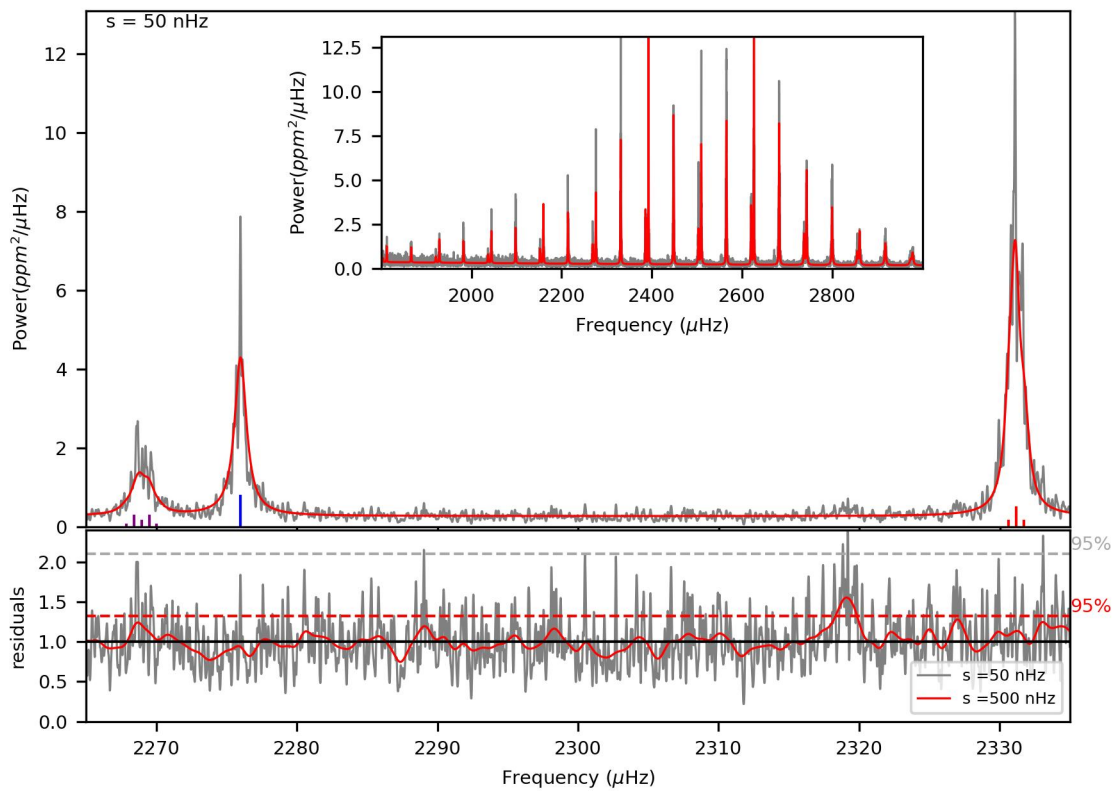


Fig. E.4. Same as Figure E.1 but for 16 Cyg B, $a_4 < -21$ nHz. Top. Highlight of a $l = 2, 0, 1$ mode group (left to right) and their fit (red). A mild power asymmetry is seen on the $l = 2$ data. Inset. Overall view of the power spectrum. Bottom. Residual of the fit with two level s of gaussian smoothing. The residual show an excess of power due to the low HNR ≈ 1.6 ($l = 3$ not fitted here).

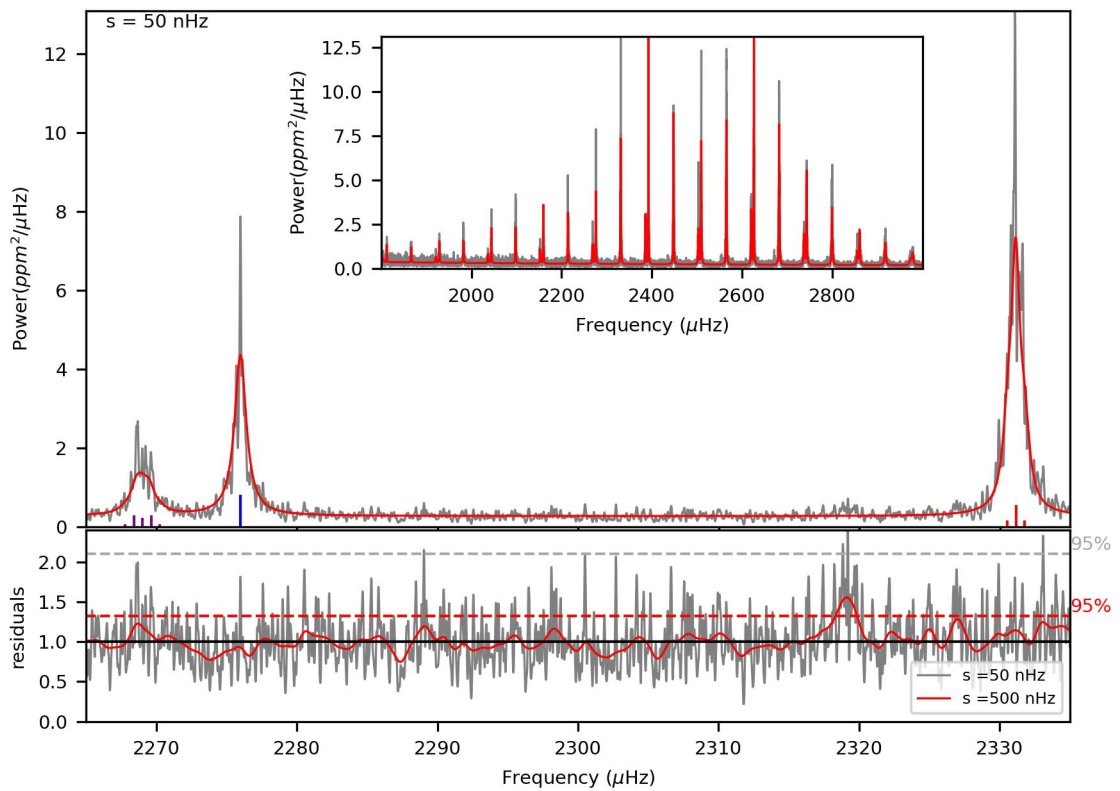


Fig. E.5. Same as Figure E.1 but for 16 Cyg B, $a_4 > -21 \text{ nHz}$. Top. Highlight of a $l = 2, 0, 1$ mode group (left to right) and their fit (red). Inset. Overall view of the power spectrum. Bottom. Residual of the fit with two level s of gaussian smoothing. The residual show an excess of power due to the low HNR ≈ 1.6 $l = 3$ (not fitted here).

References	866
Anderson, E. R., Duvall, Jr., T. L., & Jefferies, S. M. 1990, ApJ, 364, 699	867
Antia, H. M., Chitre, S. M., & Thompson, M. J. 2000, A&A, 360, 335	868
Appourchaux, T. 2003, A&A, 412, 903	869
Appourchaux, T., Antia, H. M., Benomar, O., et al. 2014, A&A, 566, A20	870
Appourchaux, T., Gizon, L., & Rabello-Soares, M.-C. 1998, A&AS, 132, 107	871
Appourchaux, T., Michel, E., Auvergne, M., et al. 2008, A&A, 488, 705	872
Atchadé, Y. F. 2006, Methodology and Computing in Applied Probability, 8, 235	873
Baglin, A., Auvergne, M., Barge, P., et al. 2006, in ESA Special Publication, Vol. 1306, ESA Special Publication, ed.	874
M. Fridlund, A. Baglin, J. Lochard, & L. Conroy, 33	875
Ballot, J., Barban, C., & van't Veer-Menneret, C. 2011, A&A, 531, A124	876
Bazot, M. 2020, A&A, 635, A26	877
Bazot, M., Benomar, O., Christensen-Dalsgaard, J., et al. 2019, A&A, 623, A125	878
Bellinger, E. P., Basu, S., Hekker, S., & Ball, W. H. 2017, ApJ, 851, 80	879
Benomar, O. 2008, Communications in Asteroseismology, 157, 98	880
Benomar, O., Appourchaux, T., & Baudin, F. 2009, A&A, 506, 15	881
Benomar, O., Bazot, M., Nielsen, M. B., et al. 2018a, Science, 361, 1231	882
Benomar, O., Bedding, T. R., Stello, D., et al. 2012, ApJ, 745, L33	883
Benomar, O., Goupil, M., Belkacem, K., et al. 2018b, ApJ, 857, 119	884
Benomar, O., Takata, M., Shibahashi, H., Ceillier, T., & García, R. A. 2015, MNRAS, 452, 2654	885
Bishop, C. M. 1995, Neural Networks for Pattern Recognition (Oxford University Press, Inc)	886
Borucki, W. J., Koch, D., Basri, G., et al. 2010, Science, 327, 977	887
Brun, A. S. & Browning, M. K. 2017, Living Reviews in Solar Physics, 14, 4	888
Buldgen, G., Farnir, M., Eggenberger, P., et al. 2022, A&A, 661, A143	889
Buldgen, G., Reese, D. R., & Dupret, M. A. 2015, A&A, 583, A62	890
Campante, T. L., Handberg, R., Mathur, S., et al. 2011, A&A, 534, A6	891
Campante, T. L., Lund, M. N., Kuszlewicz, J. S., et al. 2016, ApJ, 819, 85	892
Catura, R. C., Acton, L. W., & Johnson, H. M. 1975, ApJ, 196, L47	893
Ceillier, T., Tayar, J., Mathur, S., et al. 2017, A&A, 605, A111	894
Chandrasekhar, S. 1969, Ellipsoidal figures of equilibrium	895
Chaplin, W. J., Elsworth, Y., Isaak, G. R., et al. 2003, Monthly Notices of the Royal Astronomical Society, 343, 343	896
Cochran, W. D., Hatzes, A. P., Butler, R. P., & Marcy, G. W. 1997, ApJ, 483, 457	897
Davies, G. R., Chaplin, W. J., Farr, W. M., et al. 2015, MNRAS, 446, 2959	898
Deal, M., Richard, O., & Vauclair, S. 2015, A&A, 584, A105	899
Deheuvels, S., Doğan, G., Goupil, M. J., et al. 2014, A&A, 564, A27	900
Deheuvels, S., García, R. A., Chaplin, W. J., et al. 2012, ApJ, 756, 19	901
Deliyannis, C. P., Cunha, K., King, J. R., & Boesgaard, A. M. 2000, AJ, 119, 2437	902
Duvall, Jr., T. L., Jefferies, S. M., Harvey, J. W., Osaki, Y., & Pomerantz, M. A. 1993, ApJ, 410, 829	903
Dziembowski, W. A., Goode, P. R., Kosovichev, A. G., & Schou, J. 2000, ApJ, 537, 1026	904
Farnir, M., Dupret, M. A., Buldgen, G., et al. 2020, A&A, 644, A37	905
Frohlich, C., Andersen, B. N., Appourchaux, T., et al. 1997, Sol. Phys., 170, 1	906
García, R. A., Hekker, S., Stello, D., et al. 2011a, MNRAS, 414, L6	907
García, R. A., Salabert, D., Ballot, J., et al. 2011b, Journal of Physics Conference Series, 271, 012049	908
Gehan, C., Mosser, B., Michel, E., Samadi, R., & Kallinger, T. 2018, A&A, 616, A24	909
Georgobiani, D., Kosovichev, A. G., Nigam, R., Nordlund, Å., & Stein, R. F. 2000, ApJ, 530, L139	910
Gizon, L. 2002, Astronomische Nachrichten, 323, 251	911
Gizon, L. 2006, Central European Astrophysical Bulletin, 30, 1	912

- 913 Gizon, L., Ballot, J., Michel, E., et al. 2013, Proceedings of the National Academy of Science, 110, 13267
- 914 Gizon, L., Sekii, T., Takata, M., et al. 2016, Science Advances, 2, e1601777
- 915 Gizon, L. & Solanki, S. K. 2003, ApJ, 589, 1009
- 916 Gizon, L. & Solanki, S. K. 2004, Sol. Phys., 220, 169
- 917 Gough, D. O. & Taylor, P. P. 1984, Mem. Soc. Astron. Italiana, 55, 215
- 918 Gough, D. O. & Thompson, M. J. 1990, MNRAS, 242, 25
- 919 Gregory, P. C. 2005, Bayesian Logical Data Analysis for the Physical Sciences: A Comparative Approach with ‘Mathematical’ Support
- 920 Handberg, R. & Campante, T. L. 2011, A&A, 527, A56
- 921 Hansen, C. J., Cox, J. P., & van Horn, H. M. 1977, ApJ, 217, 151
- 922 Hartmann, L. & Rosner, R. 1979, ApJ, 230, 802
- 923 Harvey, J. 1985, ESA SP, 235, 199
- 924 Hogg, D. W., Myers, A. D., & Bovy, J. 2010, ApJ, 725, 2166
- 925 Huber, D., Bedding, T. R., Stello, D., et al. 2011, ApJ, 743, 143
- 926 Jeffreys, H. 1961, Theory of Probability, 3rd edn. (Oxford, England: Oxford)
- 927 Kamiaka, S., Benomar, O., & Suto, Y. 2018, \mnras, 479, 391
- 928 King, J. R., Deliyannis, C. P., Hiltgen, D. D., et al. 1997, AJ, 113, 1871
- 929 Libbrecht, K. G. & Woodard, M. F. 1990, Nature, 345, 779
- 930 Lignières, F., Rieutord, M., & Reese, D. 2006, A&A, 455, 607
- 931 Lund, M. N., Lundkvist, M., Silva Aguirre, V., et al. 2014, A&A, 570, A54
- 932 Lund, M. N., Silva Aguirre, V., Davies, G. R., et al. 2017, ApJ, 835, 172
- 933 Maeder, A. & Meynet, G. 2008, in Astronomical Society of the Pacific Conference Series, Vol. 388, Mass Loss from Stars and the Evolution of Stellar Clusters, ed. A. de Koter, L. J. Smith, & L. B. F. M. Waters, 3
- 934 Maia, M. T., Meléndez, J., Lorenzo-Oliveira, D., Spina, L., & Jofré, P. 2019, A&A, 628, A126
- 935 Mathur, S., García, R. A., Régulo, C., et al. 2010, A&A, 511, A46
- 936 Metcalfe, T. S., Chaplin, W. J., Appourchaux, T., et al. 2012, ApJ, 748, L10
- 937 Metcalfe, T. S., Egeland, R., & van Saders, J. 2016, ApJ, 826, L2
- 938 Morel, T., Creevey, O. L., Montalbán, J., Miglio, A., & Willett, E. 2021, A&A, 646, A78
- 939 Mosser, B., Goupil, M. J., Belkacem, K., et al. 2012, A&A, 540, A143
- 940 Neckel, H. 1986, A&A, 159, 175
- 941 Nielsen, M. B., Schunker, H., Gizon, L., Schou, J., & Ball, W. H. 2017, A&A, 603, A6
- 942 Nigam, R. & Kosovichev, A. G. 1998, ApJ, 505, L51
- 943 Nsamba, B., Cunha, M. S., Rocha, C. I. S. A., et al. 2022, MNRAS[arXiv:2205.04972]
- 944 Oláh, K., Kővári, Z., Petrovay, K., et al. 2016, A&A, 590, A133
- 945 Oláh, K., Kolláth, Z., Granzer, T., et al. 2009, A&A, 501, 703
- 946 Ouazzani, R. M., Marques, J. P., Goupil, M. J., et al. 2019, A&A, 626, A121
- 947 Papini, E. & Gizon, L. 2019, Frontiers in Astronomy and Space Sciences, 6
- 948 Pijpers, F. P. 1997, A&A, 326, 1235
- 949 Pijpers, F. P. 1998, Ap&SS, 261, 17
- 950 Ramírez, I., Meléndez, J., & Asplund, M. 2009, A&A, 508, L17
- 951 Rauer, H., Catala, C., Aerts, C., et al. 2014, Experimental Astronomy, 38, 249
- 952 Ricker, G. R., Winn, J. N., Vanderspek, R., et al. 2014, in Society of Photo-Optical Instrumentation Engineers (SPIE) Conference Series, Vol. 9143, Proc. SPIE, 914320
- 953 Ritzwoller, M. H. & Lavelle, E. M. 1991, ApJ, 369, 557
- 954 Roxburgh, I. W. 2017, A&A, 604, A42
- 955 Schou, J., Christensen-Dalsgaard, J., & Thompson, M. J. 1994, ApJ, 433, 389
- 956 Schuler, S. C., Cunha, K., Smith, V. V., et al. 2011, ApJ, 737, L32
- 957 Silva-Valio, A., Lanza, A. F., Alonso, R., & Barge, P. 2010, A&A, 510, A25

Simon, T., Ayres, T. R., Redfield, S., & Linsky, J. L. 2002, ApJ, 579, 800	961
Stahn, T. 2010, PhD thesis, Georg August University of Gottingen, Germany	962
Takeda, Y. 2005, PASJ, 57, 83	963
Thompson, M. J., Christensen-Dalsgaard, J., Miesch, M. S., & Toomre, J. 2003, ARA&A, 41, 599	964
Toutain, T., Appourchaux, T., Frohlich, C., et al. 1998, in ESA Special Publication, Vol. 418, Structure and Dynamics of the Interior of the Sun and Sun-like Stars, ed. S. Korzennik, 973	965
Toutain, T. & Gouttebroze, P. 1993, A&A, 268, 309	966
Toutain, T. & Kosovichev, A. G. 2001, in ESA Special Publication, Vol. 464, SOHO 10/GONG 2000 Workshop: Helio- and Asteroseismology at the Dawn of the Millennium, ed. A. Wilson & P. L. Pallé, 123–126	967
Ulrich, R. K. 1986, ApJ, 306, L37	968
Unno, W., Osaki, Y., Ando, H., Saio, H., & Shibahashi, H. 1989, Nonradial Oscillations of Stars (University Tokyo Press)	969
van Saders, J. L., Ceillier, T., Metcalfe, T. S., et al. 2016, Nature, 529, 181	970
Vaughan, A. H. 1983, in Solar and Stellar Magnetic Fields: Origins and Coronal Effects, ed. J. O. Stenflo, Vol. 102, 113–131	971
Verma, K., Faria, J. P., Antia, H. M., et al. 2014, ApJ, 790, 138	972
Walker, G., Matthews, J., Kuschnig, R., et al. 2003, PASP, 115, 1023	973
White, S. M. 1999, Sol. Phys., 190, 309	974
White, S. M., Iwai, K., Phillips, N. M., et al. 2017, Sol. Phys., 292, 88	975
White, T. R., Bedding, T. R., Stello, D., et al. 2011, ApJ, 743, 161	976
White, T. R., Huber, D., Maestro, V., et al. 2013, MNRAS, 433, 1262	977